CHAPTER 7. General conclusions and future research

- The potential of optically-pumped organic thin film lasers for different applications (Spectroscopy, Optical communications and Sensing) has been demonstrated at laboratory scale. To bring these devices to real market further improvements are still needed, mainly in relation to the active material, which should be simultaneously photostable, show low threshold as to enable pumping with a compact low-cost source, emit light of different colors and show good processability properties.

- The applicability of DFB lasers based on active films of PS doped with a perylene dye for sensing applications has been demonstrated. The prepared devices, which show low thresholds and high photostabilities, have shown bulk refractive index sensing capability similar to that of other DFB sensors reported and potentially sufficient for biosensing. The capability of the prepared DFB lasers for monitoring solvent extraction from the polymer film that constitutes the active film of the device when this is subjected to a thermal treatment has also been demonstrated. Particularly important has been the demonstration of the applicability of the prepared organic DFB lasers as biosensors capable to detect cancer biomarkers at relevant clinical concentrations (< 15 ng/ml).

- The DFB lasers prepared in this thesis with active films based on COPV compounds satisfy simultaneously the different requirements needed for applications: wide wavelength tunability across the visible spectrum (380-590 nm), long operational lifetimes (~10^6 pp), low threshold (0.7 kW/cm^2), processability and low fabrication cost.

- The use of COPV compounds, instead of PDIs, as active materials in DFB laser sensors might lead to a great advance towards their commercialization. On the one hand, these devices show low thresholds and prospects for pumping with compact sources. On the other hand, a blue-shifted emission (achieved with COPV*n* with n < 3) would make possible to increase their sensitivity. And finally, its high photostability could improve the sensor durability.

- The already excellent DFB performance of the devices prepared in this work could be further improved by optimizing the grating, the excitation wavelength or the polymer matrix. The novel method used in this thesis to prepare DFB gratings, by HL, on organic layers placed on top of the active films allows varying easily the grating period, key to tune the laser. The excitation wavelength used in this work could be further improved by choosing a pumping

wavelength closer to the maximum absorption and therefore, to achieve lower thresholds. New polymer matrices could reduce waveguide losses

- Exploration of energy transfer among different COPV derivatives or the use of longer COPVn with n>6 that emit at longer wavelengths will offer exciting future fields of investigation towards tunability.

CHAPTER 6. Carbon-bridged oligo(*p*-phenylenevinylene)s (COPVs) as novel laser materials

6.1 Introduction

6.2 Absorption, PL and ASE properties of COPV*n* dispersed in polymer films

6.2.1 Absorption, PL and ASE spectra of COPV*n* dispersed in polystyrene films

6.2.2 ASE threshold, PLQY and gain coefficient

6.2.3 ASE photostability

6.2.4 Effect of replacing polystyrene by poly(methyl methacrylate)

6.3 DFB lasers based on COPV*n*-based active films

6.3.1 DFB spectra

6.3.2 Threshold and photostability

6.3.3 DFB lasers with resonators on top layer over the active film

6.4 Other COPV compounds

6.4.1 COPV-IPR

6.4.2 Poly-COPV1

6.5. Conclusions

6.1 Introduction

In the introduction of this thesis we indicated that, at present, a major challenge is to find a material which shows simultaneously low threshold, long photostability and wide tunability, as well as the capability of being processed from solution-based methods. In this chapter, we show that these properties are amalgamated in a novel family of compounds -COPVs- by demonstrating ASE and DFB laser devices based on thin films containing this material. In the context of sensing applications, the use of these compounds will allow improving sensor sensitivity and efficiency. More efficient devices would allow pumping with more compact sources.

It is known that for a given active material, λ_{DFB} can be tuned in a certain range by changing Λ and/or *h*. For example, for PS doped with 0.5 wt% of PDI, a tuning range of around 30 nm was achieved by changing *h*, while keeping the same Λ.[43] A similar procedure has been used to obtain lasers with COPVs emitting at any wavelength between around 370 and 600 nm.

We have studied in a first stage, the optical properties of films consisting of a thermoplastic polymer such as PS or PMMA used as passive matrix in which a COPV compound is dispersed. In this first stage, a series of six different COPV compounds denoted as COPV*n* (figure 6.1.a) with increasing number (*n*) of monomer units: COPV1, COPV2, COPV3, COPV4, COPV5 and COPV6. A representative synthetic method for COPV*n* has been previously described.[118] We have also studied other COPV derivatives COPV1-IPR and COPV2-IPR (figure 6.1.b). In a second stage, the polymer poly-COPV1 (figure 6.1.c), prepared as a neat film, was investigated. All the COPV compounds were synthesized from commercially available materials by the group of Prof. Nakamura at the University of Tokyo.

COPVs are new organic dyes which present several remarkable properties:

(I) They have a robust all-carbon skeleton, available in a homologous series made by the repetition of a basic unit,[119] which gives them high emission quantum yield in liquid solution close to unity over the whole range of visible light region (ca. 380-590 nm), as well as high stability against light irradiation and carrier injection.

(II) They possess a flat and rigid π-system that can be excited with low photoexcitation energy.[119-121]

(III) The substituents attached to the bridging carbon atoms provide them with solubility in solvents, as well as miscibility and dispersibility in matrices.

A prominent property of COPV*n* is the high film PL efficiency as well as exceptionally high stability for COPV*n* with *n* > 3. The conjugation is sufficiently efficient to delocalize charges over the two termini (see figure 6.1) and hence to stabilize the multipolarons. The stability can be ascribed also to the steric protection of the π-system against

intermolecular interactions by the *p*-octylphenyl groups (Ar). These aryl groups are responsible for the high solubility of COPV derivatives in organic solvents (an unusual property among such highly conjugated flat π-systems).

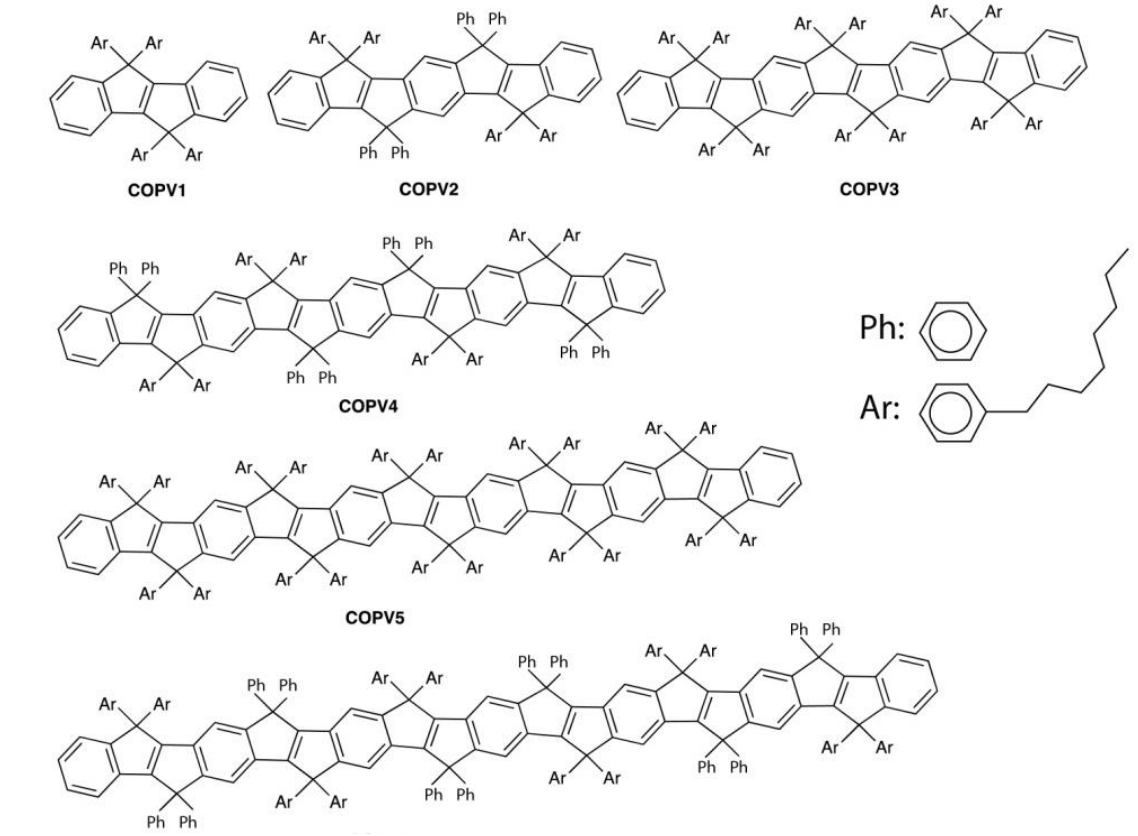

a)

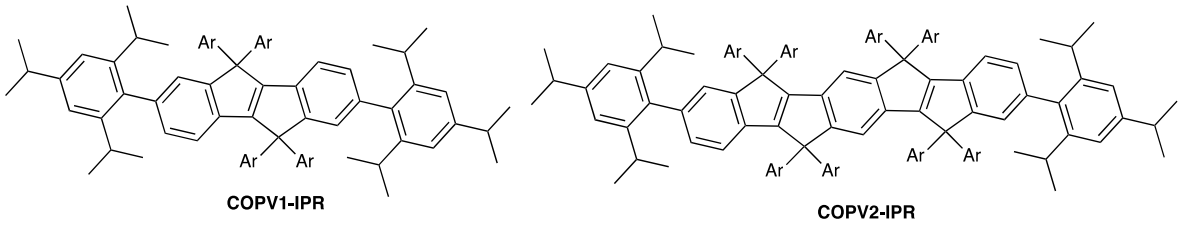

b)

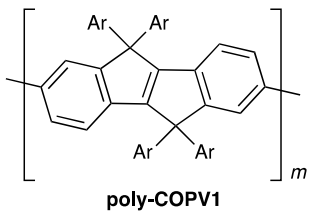

c)

Figure 6.1.- Chemical structure of COPV derivatives investigated: a) COPV*n* derivatives with *n* = 1 to 6, $R_1 = R_2 = R_3 = R_7 = R_8 = R_9 = H$, the rest of the R groups are either aryl or phenyl as shown. b) COPV1-IPR and COV2-IPR; c) Poly-COPV1 (molecular weight, Mw = 14500 g/mol).

6.2 Absorption, PL and ASE properties of COPV*n* dispersed in polymer films

6.2.1 Absorption, PL and ASE spectra of COPV*n* dispersed in polystyrene films

Given the oligomeric character of the COPV*n* compounds (*n* = 1 to 6), the molecular extinction coefficients (ε) increase with *n* (ε values measured in dichloromethane at the wavelength of maximum absorbance vary from 1.39 to 18.6 ($\times$ 10^4 $cm^{-1}M^{-1}$).[118] So, to prepare films with the different compounds and with similar absorption at a similar wavelength, larger doping ratios will be needed with the shorter oligomers (table 6.1 and figure 6.2). The ABS, PL and ASE spectra of COPV*n* (*n* = 1 to 6) dispersed in PS films are shown in figure 6.2.

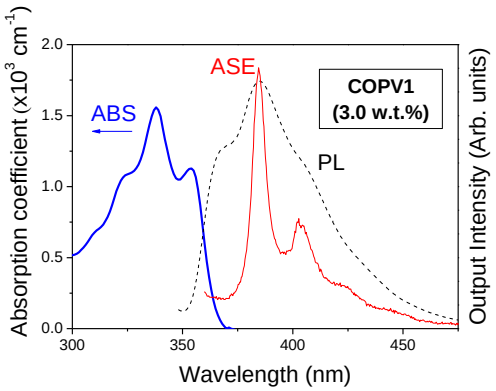

a)

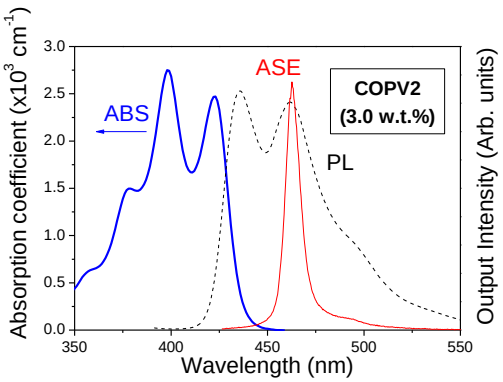

b)

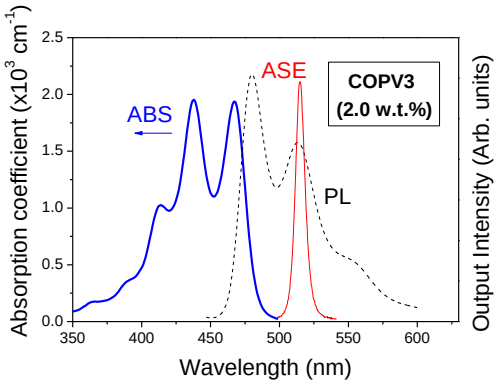

c)

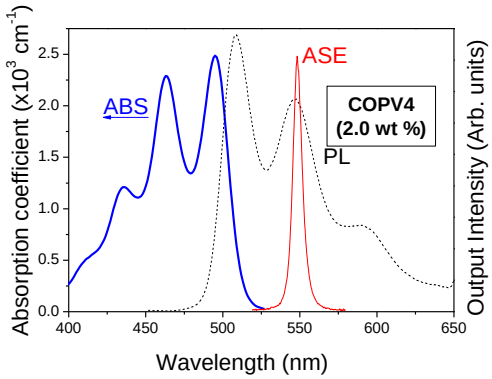

d)

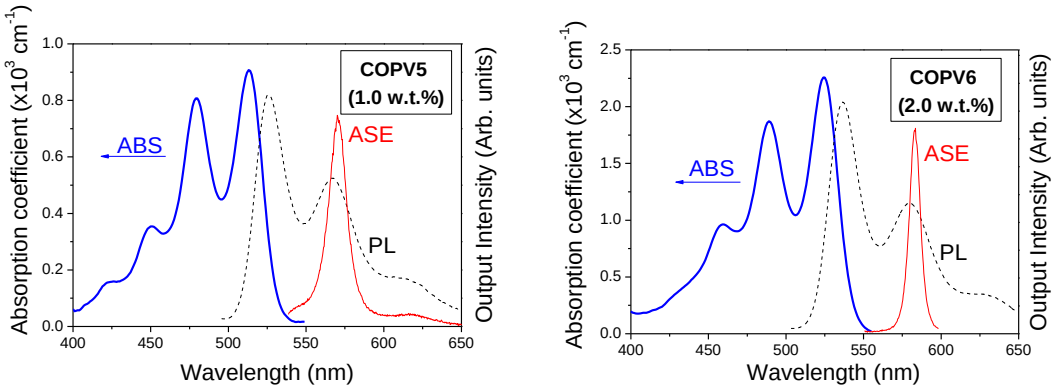

e) f)

Figure 6.2.- a) to f) show the absorbance (ABS, thick solid line, left axis), photoluminescence (PL) and ASE (dashed line and thin solid line, respectively; right axis) spectra for PS films containing a COPV*n* derivative, for *n* = 1 to 6, respectively (doping rate indicated in the legend), deposited over bare fused silica substrates (without gratings).

In order to illustrate how ASE emission allows covering the whole visible spectrum, all the ASE spectra have been plotted together in figure (figure 6.3), being the ASE linewidth around 6-9 nm for all compounds. The ASE emission appears from 385 nm in COPV1, up to 583 nm in COPV6 (figure 6.3). The tunability of λ_{ASE} by way of a simple change in the number of repeating units of conjugation (figure 6.1) represents a unique aspect of the COPV dye system compared to the conventional dye tuning strategy, in which entirely different chemical structures are needed to cover a wide range of visible light. For example with PDIs showing good laser performances, only the spectral range between 580 - 620 nm can be covered.[49,51] A similar strategy of tuning the laser wavelength by changing the number of repeating units has been employed for some structurally flexible π-conjugated oligomers[95] and polymers.[97] In those cases, the increase in the oligomer length also resulted in an increase of their structural mobility, reducing significantly their chemical stability, and hence impeding their ASE thresholds and lifetimes.

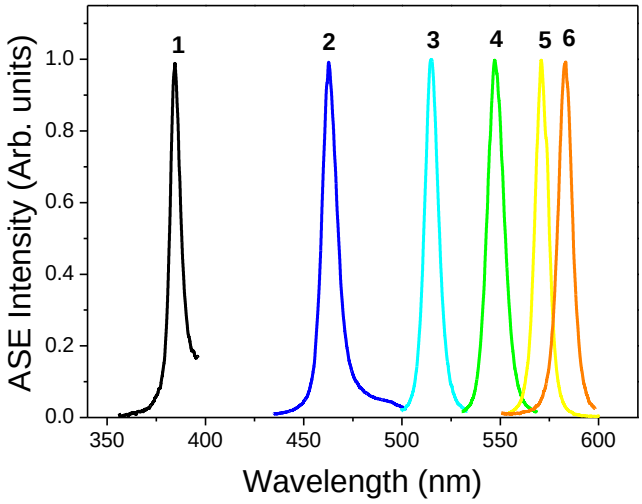

Figure 6.3.- ASE spectra for all COPV*n* compounds to illustrate coverage of the whole visible spectrum.

6.2.2 ASE threshold, PLQY and gain coefficient

ASE thresholds, $I_{th\text{-}ASE}$, for COPV*n* (*n* = 1 - 6) PS films are shown in figure 6.4. They were determined as described in section 4.3.2. Data show the existence of an inverse correlation between the absorption coefficient at the pump wavelength, $\alpha[\lambda_{pump}]$, and $I_{th\text{-}ASE}$; all data except for COPV1-2 and highly doped COPV4 and COPV6 (larger $\alpha[\lambda_{pump}]$) are aligned on the same slope. This correlation between $\alpha[\lambda_{pump}]$ and $I_{th\text{-}ASE}$ support the difference between COPV1-2 and COPV3-6 (see figure 6.4 and table 6.1).

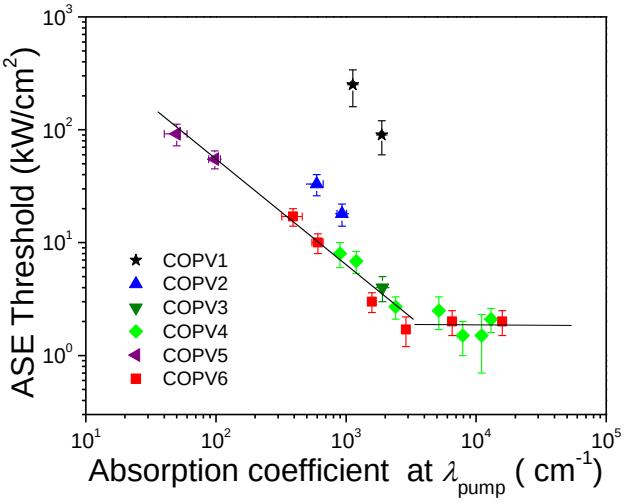

Figure 6.4.- ASE thresholds ($I_{th\text{-}ASE}$) for PS films containing COPV*n*, for *n* = 1 to 6, versus the absorption coefficient at the pump wavelength, λ_{pump}, $\alpha[\lambda_{pump}]$. The full line is a guide to the eye to show the behavior trend for COPV3–6. Errors in $\alpha[\lambda_{pump}]$ and $I_{th\text{-}ASE}$ were estimated statistically as the standard deviation from measurements on several nominally identical samples.

The PL quantum yield (PLQY) for all COPV*n* derivatives in PS films remains, as in solution,[118] extremely high (>90%) up to 5 wt% (see table 6.1) and decrease for higher doping rates (see data for COPV2, COPV4 and COPV6 in figure 6.5) suggesting that the fluorescence quenching, is because of intermolecular aggregation. The PLQY decrease obtained in COPV4 and COPV6 at high dye concentration explains the observed saturation in $I_{th\text{-}ASE}$ at these concentrations (figure 6.4).

COPV*n*	[a]COPV*n* (wt%) in matrix	[b]Matrix	[c]*h* (μm)	[d]PLQY (%)	[e]l_{pump} (nm)	[e]$\alpha[l_{pump}]$ (cm^{-1})	[g]λ_{ASE} (nm)	[h]$I_{th\text{-}ASE}$ (kW/cm^2)	[i]$\tau_{1/2}^{ASE}$ Soft pump (pump pulses)	[j]$\tau_{1/2}^{ASE}$ Strong pump (pump pulses)	[k]$FWHM_{ASE}$ (nm)
1	3.0	PS	0.61	100	355	1.13×10^3	384.5	250	1.2×10^2	-	7
	5.0	PS	0.72	100		1.88×10^3	385.2	90	1.8×10^2	-	6
1-IPR	4.2	PS	0.59	100		1.7×10^3	404.0	150	$*1.2\times10^3$	-	12
	6.9	PS	0.77	95		3.0×10^3	404.7	70	$*6.0\times10^2$	-	9
2	3.0	PS	0.61	100	355	6.0×10^2	462.7	33	1.7×10^4	1.2×10^3	9
									$*7.2\times10^3$		
	5.0	PS	0.68	100		9.3×10^2	464.0	18	1.6×10^4	-	6
									$*3.6\times10^3$		
	10.0	PS	0.62	0.96		2.1×10^3	464.0	10	6.0×10^3	-	6
	20.0	PS	0.64	0.88		4.5×10^3	464.0	6	3.0×10^3	-	5
2-IPR	3.8	PS	0.64	100		5.7×10^2	473.8	61	$*1.4\times10^4$	-	8
	6.9	PS	0.76	94		8.0×10^2	475.1	19	$*9.0\times10^3$	-	9
3	2.0	PS	0.65	100	436	1.91×10^3	514.8	4.0	8.4×10^4	6.0×10^3	8
4	2.0	PS	0.63	100	436	1.2×10^3	548.2	7	1.9×10^5	1.3×10^4	7
	2.0	PMMA	1.16	100		1.2×10^3	544.6	7	1.8×10^5	1.3×10^4	7
	5.0	PS	0.60	100		2.4×10^3	549.2	2.7	1.4×10^5	1.0×10^4	8
	10.0	PS	0.65	94		5.1×10^3	550.8	2.5	1.1×10^5	7.9×10^3	7
	15.0	PS	0.53	85		7.9×10^3	552.2	1.5	8.0×10^4	5.6×10^3	7
	20.0	PS	0.56	77		1.1×10^4	552.8	1.5	5.6×10^5	3.9×10^3	7
	20.0	PMMA	0.49	-		1.1×10^4	552.2	1.8	3.0×10^4	2.1×10^3	7
5	0.5	PS	0.63	100	532	50	571.1	90	3.0×10^5	1.8×10^4	8
	1.0	PS	0.62	100		1.0×10^2	571.8	55	3.7×10^5	2.2×10^4	8
6	0.5	PS	0.62	100	532	3.9×10^2	582.4	17	7.7×10^5	5.1×10^4	8
	1.0	PS	0.64	94		6.1×10^2	582.7	10	7.5×10^5	4.7×10^4	9

	2.0	PS	0.69	99		1.6×10^3	583.4	3.0	9.6×10^5	5.0×10^4	8
	4.0	PS	0.77	94		2.89×10^3	583.7	1.7	3.6×10^5	2.4×10^4	8
	8.0	PS	0.52	78		6.5×10^3	584.4	2.5	1.2×10^5	1.3×10^4	7
	20.1	PS	0.49	40		1.59×10^4	585.0	2.0	3.5×10^4	2.5×10^3	6
Poly-COPV1	neat	No	0.25	68	450	6.67×10^4	527.3	4.0	7.7×10^4	-	5

Table 6.1.- Optical and ASE parameters of devices based on COPV. [a]Error ~ 0.1 wt%; [b]PS: polystyrene film, PMMA: poly (methylmetacrylate); [c]Film thickness (error ~5%); [d]Photoluminescence quantum yield (errors for COPV6 films in figure 6.5); [e]Pump wavelength; [f]Absorption coefficient at the pump wavelength (errors in figure 6.4); [g]ASE wavelength (error is $\pm$0.5 nm); [h]ASE threshold (errors in figure 6.4, estimated from measurements on several nominally identical samples); [i]ASE photostability half-life under I_{pump}~ ($2 \times I_{th\text{-}ASE}$), except those with * for which I_{pump}~ 200 kW/cm^2 , at 10 Hz pump (error ~ 10%, estimated as in [g]); [j]Same as [h], but at $I_{pump} = 2.5\times10^3$ kW/cm^2;[k]ASE linewidth (error is $\pm$1 nm).

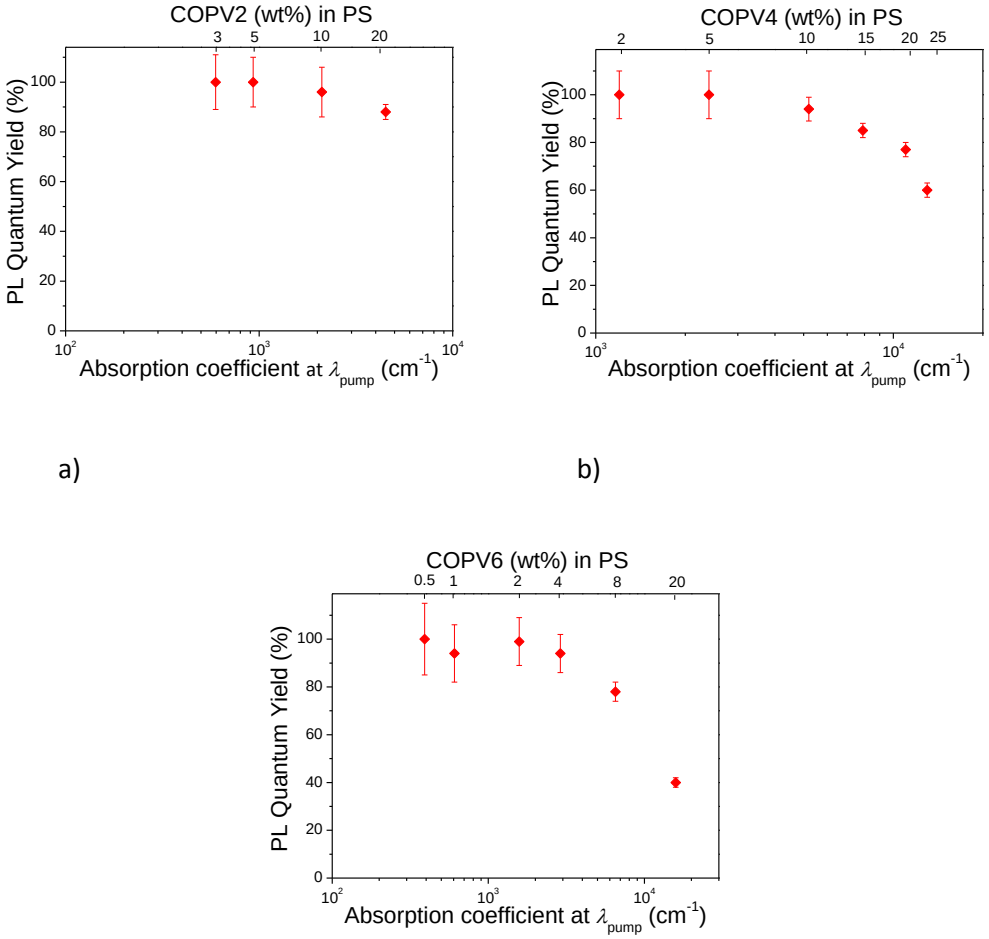

Figure 6.5.- Film PLQY for: a) COPV2; b) COPV4 and c) COPV6 versus absorption coefficient at the pump wavelength λ_{pump}, and versus dye concentration (bottom and top axes, respectively). Errors in PLQY were estimated statistically as the standard deviation from measurements on several nominally identical samples.

The net gain coefficient (gain minus losses), g_{net} (see section 4.3.2), at two different pump intensities, for an 8 wt% COPV6 doped PS film were obtained from plots of the output intensity versus the length of the excitation stripe figure 6.6. The g_{net} values obtained have been 60 and 6.3 cm^{-1}, at pump intensities of 43.3 and 11.5 kW/cm^2, respectively. Data have been fitted with eq. 1.8 by using AI_p values of 2.60 and 0.86, respectively. Gain saturation is present in the curve obtained at the higher pump intensity (43.3 kW/cm^2), so only points obtained at short excitation lengths were used for the fit.

These g_{net} values are much superior to those obtained with other *p*-phenylenevinylene oligomers (g_{net} = 13 cm^{-1} at I_{pump} = 55 kW/cm^2)[96] and PDIs dispersed in PS (g_{net} = 8 cm^{-1} at I_{pump} = 60 kW/cm^2)[122] and only about twice lower than state-of-the-art organic semiconductors.[4,123]

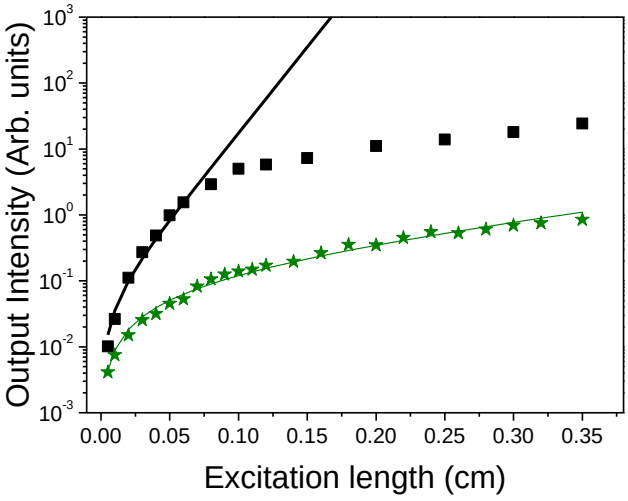

Figure 6.6.- The dependence of the emission intensity at λ = 584 nm on the excitation length, at pump intensities of 43.3 and 11.5 kW/cm^2 (squares and stars respectively). The solid lines are fits to the data using eq. (1.8) with AI_p values of 2.60 and 0.86 (in arbitrary units); and net gain coefficients, g_{net}, of 60 and 6.3 cm^{-1}, respectively.

6.2.3 ASE photostability

A remarkable property of COPV*n* is their excellent ASE photostability under ambient conditions. For a 2 wt% COPV6 doped PS film (figure 6.7), the ASE intensity remained unchanged after 3.5 $\times$ 10^5 pp (ca. 8 h). Its ASE photostability half-life ($\tau_{1/2}^{ASE}$) was around 1 $\times$ 10^6 pp (>24 h) under soft pumping (SP) conditions, that is under pump intensity (I_{pump}) only twice that of $I_{th\text{-}ASE}$ (3 kW/cm^2, or 600 nJ/pulse). This photostability is in stark contrast to that of flexible counterparts of COPVs such as phenylenevinylene oligomers[96] and polymers,[4,9] whose ASE under ambient conditions lasts for just a few minutes. Moreover, the photostability of COPV6 in PS films is even better than the best results reported for aromatic laser dyes doped in a polymer matrix.[46,49-51,86] The high photostability of COPV*n* was further attested by an experiment pumping COPV6 with an extremely intense light (figure 6.7), denoted here as exteme pump (EP) conditions (I_{pump} = 2.5 x 10^3 kW/cm^2 ~10^3 times more intense than its threshold), where $\tau_{1/2}^{ASE}$ decreased only by a factor of 20 (5.5 x 10^4 pp, ca. 92 min).

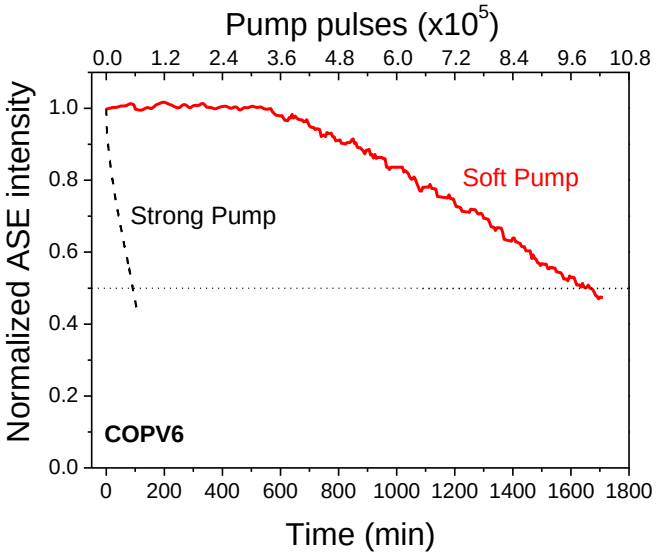

Figure 6.7.- ASE intensity versus time, and versus the number of pump pulses (bottom and top axes, respectively) for a 2 wt% COPV6-doped PS film deposited over a bare fused silica substrate under soft pump (full line, pump intensity 2 times above the ASE threshold) or strong pump (dashed line, pump intensity 1000 times above threshold) conditions.

Dye laser photostability, which is partly related to intermolecular degradation pathways, depends on the concentration of the dye in a polymer matrix, that is, on the absorption coefficient at the pump wavelength, $\alpha[\lambda_{pump}]$, as has been observed in PDIs dispersed in PS and PMMA.[50-51] As observed in samples based on COPV6 (see figure 6.8) no significant differences in $\tau_{1/2}^{ASE}$ are found in the range 0.5 – 2 wt%. However, the half-life $\tau_{1/2}^{ASE}$ decreases when $\alpha[\lambda_{pump}]$ increases between 4 and 20 wt%, but even at heavy doping rates as great as 20 wt%, the lifetime is still long ($\tau_{1/2}^{ASE} = 3.5 \times 10^4$ pp).

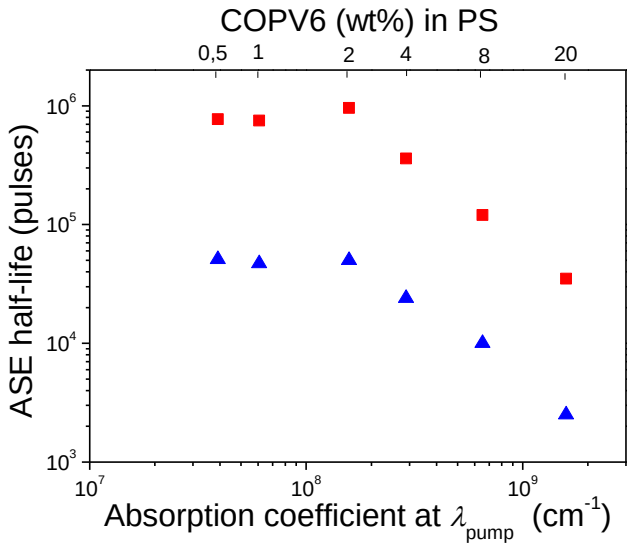

Figure 6.8.- ASE photostability half-life, $\tau_{1/2}^{ASE}$ versus the absorption coefficient at the pump wavelength, $\alpha[\lambda_{pump}]$, of films with different COPV6 concentrations (shown on the top axis) under soft pump (■) and strong pump (▲) conditions.

On the one hand, devices based on COPV3-5 are likewise highly photostable in PS films under air at room temperature ($\tau_{1/2}^{ASE}$ ~ 10^5 pp under SP, figure 6.9), while $\tau_{1/2}^{ASE}$ decreases gradually from COPV6 to COPV3. We consider that the high photostabilities of COPV3-6 reflect the robustness of their excited states, a properly probably originating from the steric protection and the effective π-conjugation, as demonstrated by Raman spectroscopy of the neutral and cationic COPVs.[124]

On the other hand, the photostability decreases significantly for COPV1 and COPV2, probably because of their high photoexcited state energy. COPV1 decomposed too quickly under soft pumping conditions to be studied for its half-life. The half-life $\tau_{1/2}^{ASE}$ of COPV1 and COPV6 doubled under a nitrogen atmosphere, suggesting that the degradation process involves oxidation of the dye molecules on the most reactive terminal sites, not through the *p*-octylphenyl-protected π-surface. Taken together with the threshold data and the adverse effects of molecular oxygen for ASE, we suggest that the higher $I_{th\text{-}ASE}$ values and the short operational lifetimes of COPV1 and COPV2 are related to the activation of the excited state to photoreaction through the unprotected terminal positions similarly to the reaction with molecular oxygen.

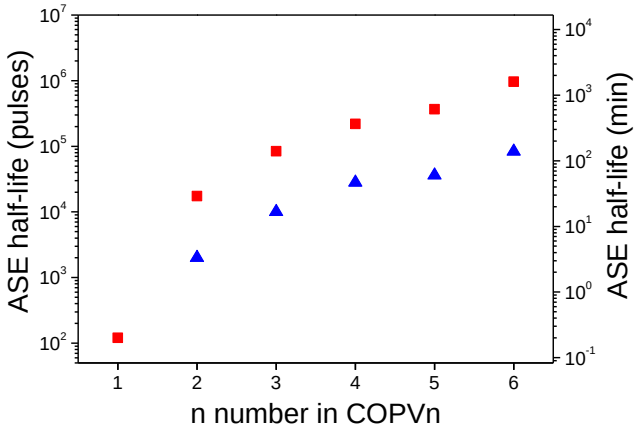

Figure 6.9.- Shows ASE photostability half-lives, $\tau_{1/2}^{ASE}$ for all COPV*n* (doping rates into PS are the same as in figure 6.2) under soft pump (■) and strong pump (▲) conditions.

6.2.4 Effect of replacing polystyrene by poly(methyl methacrylate)

We have explored the effect on the ASE properties of replacing PS by PMMA, as the polymer matrix to disperse COPV*n*. The PMMA film thickness used was larger (~1 µm) than that of the PS one (~0.6 µm), in order to obtain a similar confinement of the waveguide mode (the refractive index of PMMA n = 1.49 at λ = 579 nm is lower than that of PS n = 1.59 at λ = 579 nm). The ASE and DFB performances, in terms of threshold and photostability lifetime are very similar to those obtained with those based on PS (see tables 6.1 and 6.2). The only difference found is that the ASE wavelength is slightly blue shifted when using PMMA (figure 6.10) as a consequence of the different local environment for COPV*n*.

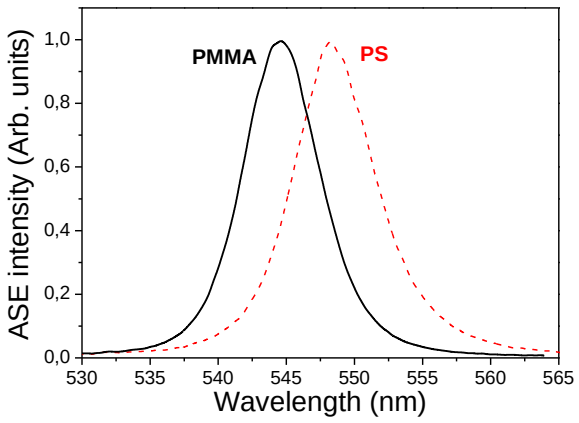

Figure 6.10- ASE spectrum of a PMMA film containing 3 wt% of COPV4 (full line), compared to the spectrum of a PS film with the same COPV4 content (dashed line).

6.3 DFB lasers based on COPV*n*-based active films

6.3.1 DFB spectra

A list of relevant geometrical and performance parameters for the various DFB lasers prepared, based on either PS or PMMA active films containing a COPV*n* derivative, are listed in table 6.2. Representative DFB spectra are shown in figure 6.11. The use of gratings engraved by different methods (thermal-NIL or HL) over substrates of different kind (i.e. SiO_2 or polymeric resists), serves to show the possibilities from the point of view of processing. At this respect, an issue of particular interest is the possibility of preparing flexible devices, for example by using polymeric substrates with gratings.

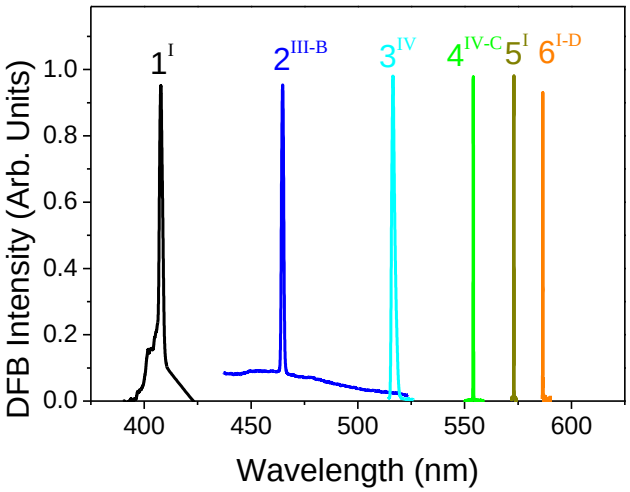

Figure 6.11.- Emission spectra of DFB lasers in which the active film is made of PS and a COPV*n* compound, for *n* = 1 to 6. Device label description: the Arabic number denotes *n*; the roman number in the superscript denotes the type of DFB device geometry according to figure 1.7 and the accompanying capital letter refers to a particular device. Device parameters (grating period and depth, active film thickness, excitation wavelength, resonator material) for all lasers are listed in table 6.2.

We focus now mainly on the best performing system, COPV6. The lasing wavelength λ_{DFB} was tuned within a spectral range of around 20 nm, centered at the wavelength of maximum gain (λ_{ASE}) by changing Λ and/or the thickness of the COPV6 film (h_f), see table 6.2 and figure 6.12.a Single mode emission was obtained in all cases with linewidths < 0.13 nm.

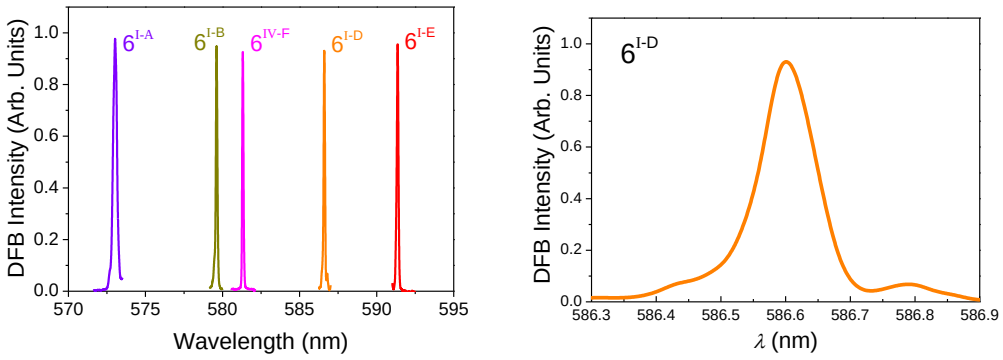

a) b)

Figure 6.12.- a) Emission spectra of various DFB lasers based on PS films containing COPV6. b) DFB spectrum for one of the lasers based on COPV6 (device $6^{I\text{-}D}$) on an expanded scale to illustrate that emission is single mode. Parameters details are shown in table 6.2.

6.3.2 Threshold and photostability

It should be noted that for the scope of this work, in which the emphasis is in the capabilities of the active material, we have not worked towards the optimization of the laser threshold, which is known to depend on various device parameters such as number of waveguide modes, proximity of the emission wavelength to the maximum of the gain spectrum, confinement of the waveguide mode, etc.[43] This means that the threshold values shown in table 6.2, could be further improved by modifications in the device architecture.

Nonetheless, we have already obtained excellent results with DFB lasers based on COPV6. Devices based on 8 wt% COPV6-doped PS films, emitting close to λ_{ASE} (devices $6^{I\text{-}C}$ and $6^{I\text{-}D}$, Table 6.2; $6^{I\text{-}D}$ also in figure 6.12.b) have shown a $I_{th\text{-}DFB}$ as low as 0.7 ± 0.1 kW/cm^2, or 70 ± 10 nJ/pulse; a value which is the lowest among the reported DFBs based on dye doped polymer active materials, and very close to the requirements for LED pumping (~0.2-0-5 kW/cm^2).[14] In addition, these devices at a 8 wt% doping rate show operational lifetimes as long as $\tau_{1/2}^{DFB} = 1.0 \times 10^5$ pp. A COPV laser prepared with a PS film containing 2 wt% of COPV6 showed a longer lifetime (device $6^{I\text{-}B}$ in table 6.2, $\tau_{1/2}^{DFB} = 1.0 \times 10^6$ pp) at the expenses of a slightly higher threshold value of $I_{th\text{-}DFB} = 2.1 \pm 0.2$ kW/cm^2, or 210 ± 20 nJ/pulse (figure 6.13). The higher DFB threshold of device $6^{I\text{-}B}$ is mainly due to the lower COPV content. And therefore, it is consequence of the lower absorption coefficient and the higher ASE threshold as shown in figure 6.4. It is also because the separation of λ_{DFB}

from λ_{ASE} of this device is larger than that of device $6^{I\text{-}C}$ (table 6.2) as this parameter is known to have the largest influence on the threshold as we have mentioned above.

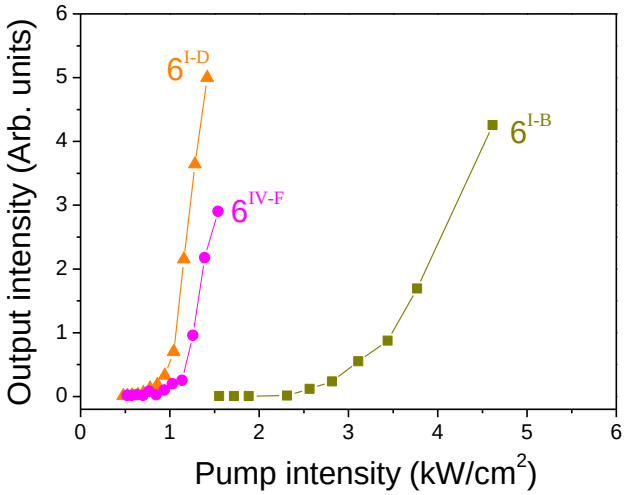

Figure 6.13.- Plots of the output intensity versus the pump intensity for various COPV6 devices (see table 6.2). Full lines are guides to the eye.

[a]COPV*n* device	Type of device	Matrix	[b]COPV*n* wt% in PS	[c]*h* (μm)	[d]Resonator material	[e]*d* (nm)	[f]Λ (nm)	[g]λ_{ASE} (nm)	[h]λ_{DFB} (nm)	[i,†]$I_{th\text{-}DFB}$ (kW/cm^2)	[j,†]$\tau_{1/2}^{DFB}$ (pp)
$6^{I\text{-}A}$	I	PS	0.5	0.62	SiO_2	95	368	582.4	573.0	11	8.0×10^5
$6^{I\text{-}B}$	I	PS	2.0	0.47	SiO_2	30	380	583.4	579.6	2.1	1.0×10^6
$6^{I\text{-}C}$	I	PS	8.0	0.49	SiO_2	75	380	584.4	586.7	0.7	1.0×10^5
$6^{I\text{-}D}$	I	PS	8.0	0.49	FS	60	380	584.4	586.6	0.7	1.1×10^5
$6^{I\text{-}E}$	I	PS	20.1	0.57	FS	60	380	585.0	591.4	0.8	1.1×10^4
$6^{IV\text{-}F}$	IV	PS	2.0	0.57	DCG	65	370	583.4	581.3	0.9	9.5×10^5
5^{I}	I	PS	1.0	0.63	SiO_2	95	368	571.1	573.1	20	4.0×10^5
$4^{IV\text{-}A}$	IV	PS	2.0	0.64	DCG	71	351	548.2	553.8	1.1	1.8×10^5
$4^{IV\text{-}B}$	IV	PMMA	2.0	1.1	DCG	86	369	544.6	548.1	1.3	1.7×10^5
$4^{IV\text{-}C}$	IV	PS	5.0	0.60	DCG	90	353	549.2	556.6	1.0	1.3×10^5
$4^{IV\text{-}D}$	IV	PS	10.0	0.56	DCG	85	349	550.8	551.0	0.6	1.1×10^5
3^{IV}	IV	PS	2.0	0.65	DCG	80	321	514.8	516.4	1.0	8.1×10^4
$2^{III\text{-}A}$	III	PS	5.0	0.65	DCG	50	308	464.0	490.9	90	4.0×10^3

2 [III-B]	III	PS	5.0	0.38	DCPVA	40	296	464.0	464.7	550	8.0×10^2
2-IPR [III-C]	III	PS	6.9	0.78	DCG	60	308	475.1	476.9	91	-
1 [I]	I	PS	3.0	0.61	Glass	70	270	384.5	407.8	>8,000	-

Table 6.2.- Summary of DFB devices based on COPV. [a]Arabic number on the label refers to *n*, the roman number in superscript refers to type of DFB device according to figure 1.7; [b]Error ~ 0.1%; [c]Film thickness (error ~ 5%); [d]FS: fused silica, SiO_2: SiO_2 layer over silicon, DCG: dichromated gelatin photoresist layer over FS, DCPVA: dichromated poly(vinyl alcohol) photoresist layer over FS; [e]Grating depth; [f]Grating period; [g]ASE wavelength (error is ±0.5 nm); [h]DFB wavelength (error is ±0.1 nm); [i]DFB threshold; [j]DFB photostability half-life under $I_{pump} \sim (2 \times I_{th\text{-}DFB})$, at 10 Hz; [†]Error ~ 10%, estimated as standard deviation from measurements on nominally identical samples.

6.3.3 DFB lasers with resonators on top layer over the active film

As we have seen in figure 6.13 and table 6.2, the threshold of a COPV-based DFB laser with a type I resonator fabricated by NIL over an inorganic substrate (device $6^{I\text{-}D}$) is similar to that of a device with a similar active film but based on a DCG resonator with type IV (device $6^{IV\text{-}F}$). Previously reported resonators made by HL on DCG with type III geometry and PDI-doped PS active materials[51-53] showed an inferior performance in comparison to similar ones based on resonators with type I geometry.[43,46-48] Therefore, the high quality of DFB devices with DCG resonator on top of the active layer (type IV), seems an important matter of study.

In order to obtain an exhaustive comparison between type I, III and IV DFBs devices, we have chosen similar film thickness and the proper grating period to obtain DFB emission close to the ASE wavelength (this is one of the most important conditions to reduce threshold as it is demonstrated below). For the purpose of this study we have chosen as active material PS doped with 1 wt% of PDI-O, the same one used in chapter 5 because this is a commercial compound available in our laboratory and there are many previous studies with it.[49] The geometrical and optical parameters of the prepared DFB lasers are shown in table 6.3. The output intensity versus pump intensity curves for the devices, from which the thresholds are determined, are shown in figure 6.14. The n_{eff} values used in this calculation were obtained by solving the propagation wave equation for the simplest possible model waveguide consisting of a film of thickness h_f deposited over a fused silica grating (n_s = 1.46 at λ = 580 nm) of infinite thickness (see section 1.3).[88,112] We have assumed that the cover layer (air) has infinite thickness. In the case of lasers with DCG grating, the n_{eff} values could not be calculated in the frame of a waveguide film between two media of infinite thickness, because of the presence of the DCG layer. Instead, a multilayer model was used.[93]

Resonator	Λ (nm)	*d* (nm)	h_f (nm)	λ_{DFB}^{exp} (nm)	$I_{th\text{-}DFB}$ (kW/cm^2)	n_{eff}	λ_{Bragg} (nm)
Fused Silica type I	376	60	600	583.4	1.3	1.5523	583.7
DCG type III	373	50	601	582.6	15	1.5575	581.0
DCG type IV	373	90	610	582.8	1.5	1.5553	580.1

Table 6.3.- Geometrical and optical parameters of DFB lasers based on 1 wt% of PDI-O-doped PS active films and different types of resonators. DCG: dichromated gelatine photoresist; the roman number refers to the type of DFB device geometry according to figure 1.7; h_f: film thickness (error ~ 5%); *d*: grating depth; Λ: grating period; λ_{DFB}^{exp}: experimental DFB wavelength (error is ±0.1 nm); $I_{th\text{-}DFB}$: DFB threshold; n_{eff}: effective refractive index; λ_{Bragg}: theoretical DFB wavelength.

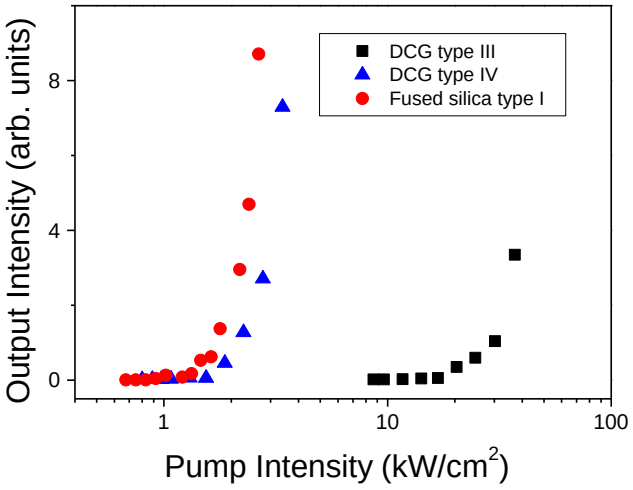

Figure 6.14.- Output intensity versus pump intensity for DFB lasers based on 1 wt% of PDI-O-doped PS active films and different types of resonators.

The DFB thresholds obtained confirm the high performance of devices based on DCG grating on top of the active film, which is similar to that obtained with high quality gratings fabricated by NIL and subsequent etching over FS substrates. In this standard DFB lasers (grating engraved on the substrate), the active material is modulated in thickness, presumably leading to an ineffective use of the gain volume. So, even though the amplitude of the modulation is usually lower than 100 nm, it would interfere with the propagation of the light, thus increasing the losses.

Despite the potential advantages of DFB lasers with type IV geometry, this has been used only in a few cases in the literature. Zhai et al[125] fabricated in 2011 a DFB laser with the resonator on top of the active layer. They discussed the advantages of that resonator, particularly its potential for the design of electrically-pumped organic DFB lasers. However, their device showed a high threshold, 230 kW/cm^2, which was attributed to a deficient procedure in which the active layer was damaged by the solvent of the resist used to make the grating. Better results were obtained by Ding et al,[126] which fabricated a DFB laser by spin coating the resist on top of an organic single crystal. Recently, organic DFB lasers fabricated via nanograting transfer have been proposed.[127,128] In these lasers a grating is deposited by microcontact molding on top in the active layer. The stamps must be brought into contact with the active layer and removed again ensuring the translation-only movement for avoiding the decrease of the grating quality. Reproducibility and control of the grating depth were not reported.

It is remarkable that in our devices the deposition of the DCG resonator on top of the active film is done without damaging the active layer. This is because the resist material used (DCG) is prepared from a water solution, while the active film is prepared from a solution in an organic solvent (toluene in this case). Furthermore, another advantage of this kind of DFB resonators is that they offer the possibility to obtain wavelength tunability in a single device, which can have several cm in size. The use of HL enables easy variation of the grating period (figure 6.15).

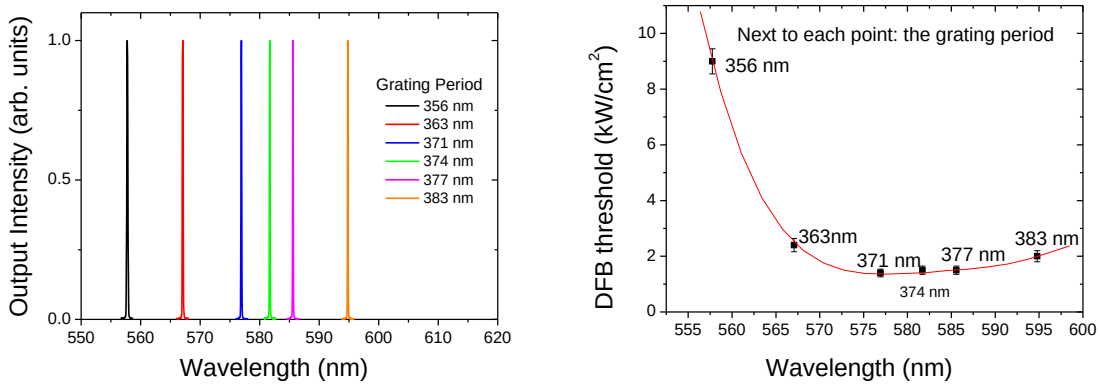

Figure 6.15.- DFB devices with DCG resonator (*d* = 90 nm) on top of the active layer (PDI-O = 1 wt%, h_f = 560 nm). a) DFB spectra, b) DFB threshold, as a function of the emission wavelength.

Figure 6.15a shows the DFB spectra obtained for devices with different grating periods, easily obtained by changing the interbeam angle during the grating recording by HL. Figure 6.15b shows, as expected, that the minimum DFB threshold is obtained when emission is close to the ASE wavelength. It also shows the emission range (575-587 nm) in which the DFB threshold is nearly constant. Therefore, the DFB threshold comparison done in table 6.3 is properly done because they are not affected by differences in the DFB emission wavelength.

6.4 Other COPV compounds

6.4.1 COPV-IPR

The derivatives COPV1-IPR and COPV2-IPR differ from the corresponding COPV1 and COPV2, in the groups attached to the terminal positions (figure 6.1). The aim of attaching the IPR substituents to COPV1 and COPV2, was to prevent photodegradation, while ideally not affecting the optical properties (ABS and PL). However, we found that these are somewhat different.

First of all, the ABS spectra of the films doped with the IPR-substituted COPVs are red-shifted with respect to those of their corresponding COPVs without IPRs, although their shapes are similar (see figure 6.16.a). It is also observed that the total ABS (area below the spectrum) of COPV1-IPR is larger than that of COPV1 and larger than that of COPV1 at λ = 355 nm. On the other hand, for COPV2 and COPV2-IPR, the absorption at λ= 355 nm is approximately the same. Note that for a proper comparison, films with the same molar concentration were used (i.e. for films doped with COPV1 and COPV2, the concentration was 3 wt%; for the IPR-substituted compounds, the percentage was adjusted to have the same molar concentration, “moles dye / g PS”, see table 6.1 for more details).

In order to ascertain whether the differences in the absorption spectra of the IPR-substituted compounds with respect to their corresponding COPVs without IPRs are due to a different behaviour of the molecules or to different intermolecular interactions, we measured absorption in diluted liquid solutions. Spectra of the molar extinction coefficient (ε) in liquid solution for the IPR compounds are shown in figure 6.16.b. For comparison purposes, results for the corresponding compounds without IPR substituents have also been included.

It is seen that for both IPR-substituted compounds, the total absorption (area below the spectrum) and the molar extinction coefficient at the wavelength of maximum intensity and at λ_{pump} are larger than those of their corresponding compounds without IPR. The same holds for COPV1-IPR at λ = 355 nm (pump wavelength to obtain ASE in these compounds), ε = 1.1×10^4 $M^{-1}cm^{-1}$, for COPV1 and ε = 2.3×10^4 $M^{-1}cm^{-1}$ for COPV1-IPR.

These results indicate that the larger absorption observed in films containing COPV1-IPR, relative to that of films doped with COPV1, is because its ε is larger. On the other hand, for COPV2 and COPV2-IPR, the molar extinction coefficient at the wavelength of maximum intensity is slightly higher, whereas at λ_{pump} this parameter is similar for both compounds, due to the spectral shift of the latter one.

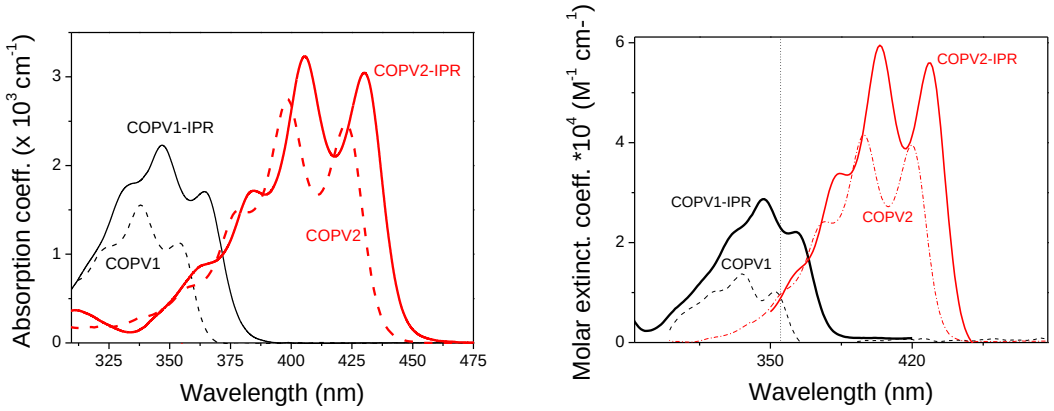

a) b)

Figure 6.16.- a) ABS spectra of PS films containing COPV1-IPR or COPV2-IPR, compared to those of films containing COPV1 and COPV2. Dye content in the COPV1 and COPV2 films is 3 wt% and percentages for COPV1-IPR and COPV2-IPR were adjusted to have the same molar concentration. b) Molar extinction coefficient for COPV-1, COPV1-IPR, COPV-2 and COPV-2-IPR measured in dichloromethane. The pump wavelength is indicated with a vertical dotted line.

Concerning the PL spectra of the films containing the IPR-substituted COPVs, they are also red-shifted with respect to their corresponding COPVs without IPR substituents (see figure 6.17). As a consequence, ASE appears at a different wavelength. The observation of these shifts in the IPR compounds might be due to an increase of conjugation. Although the conformation of the IPR substituents in the ground state is perpendicular to the COPV core, it might not be the case for the excited state. In addition, the conformation of the IPR substituents might influence the distance between neighbouring molecules, which might be important for films with high doping ratios.

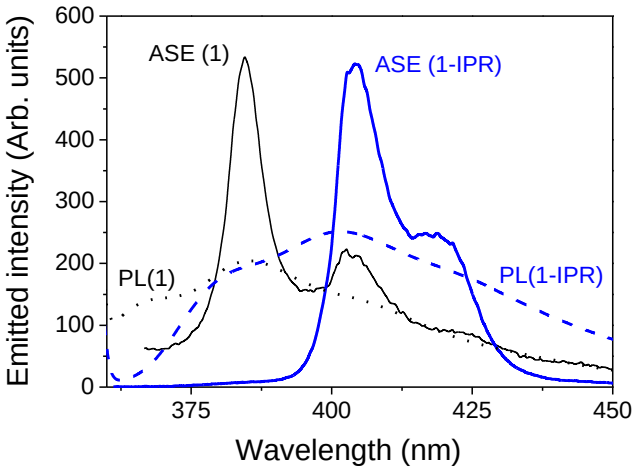

a)

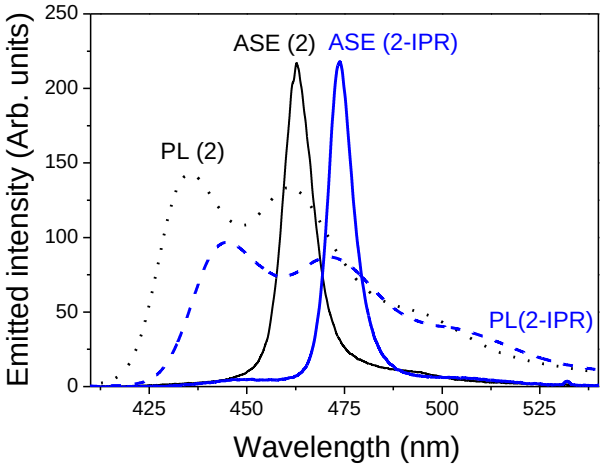

b)

Figure 6.17.- PL spectra (divided by film thickness) and ASE spectra of PS films containing a) COPV1-IPR or b) COPV2-IPR, compared to those of COPV1 and COPV2, respectively. Dye contents in the films are the same as in figure 6.16.

The ASE threshold for the film containing COPV1-IPR is by around four times lower than the one doped with COPV1 (see table 6.1). This is due to the higher absorption at the pump intensity, and therefore PL intensity of COPV1-IPR. In the case of COPV2-IPR, its ASE threshold is around two times larger than that of COPV2. In spite of the larger film ABS at the peak wavelength in COPV2-IPR, at the pump wavelength it has similar or lower ABS.

With regards to the ASE photostability of films containing COPV1-IPR or COPV2-IPR, the $\tau_{1/2}^{ASE}$ values are around 3 times larger than those of the films with the corresponding COPVs without IPRs (table 6.1). COPV1-IPR $\tau_{1/2}^{ASE}$ is also doubled under a nitrogen atmosphere (figure 6.18), as COPV1 and COPV6 (see section 6.2.3)

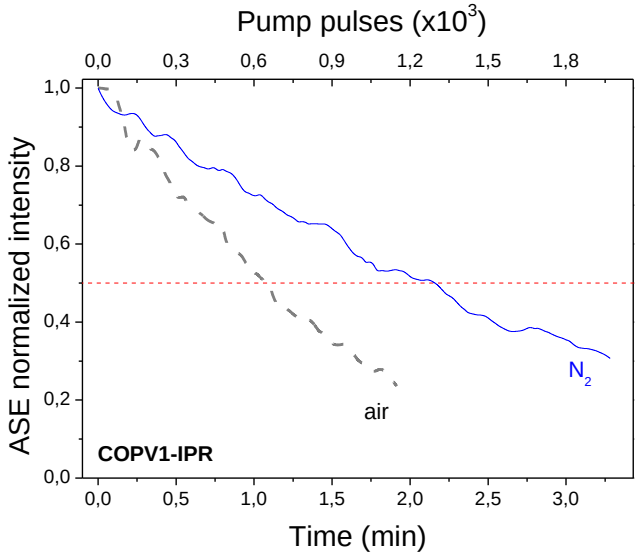

Figure 6.18.- ASE intensity versus time and versus the number of pump pulses (bottom and top axis respectively) for PS films doped with COPV1-IPR, under air (grey dashed line) and under N_2 atmosphere (blue full line). Samples have been excited continuously at a pump intensity of 200 kW/cm^2.

The use of COPV-IPRs for DFB laser fabrication is illustrated by the preparation of a device based on COPV2-IPR (see table 6.2).

6.4.2 Poly-COPV1

The optical performance of a neat film of poly-COPV1 (figure 6.19) was explored during a short stay in St. Andrews University. Since in this case the compound is not diluted in a matrix, film absorbance $\alpha[I_{pump}]$ is significantly higher, more than one order of magnitude higher than that obtained with films based on COPV*n* dispersed in PS or PMMA (see table 6.1).

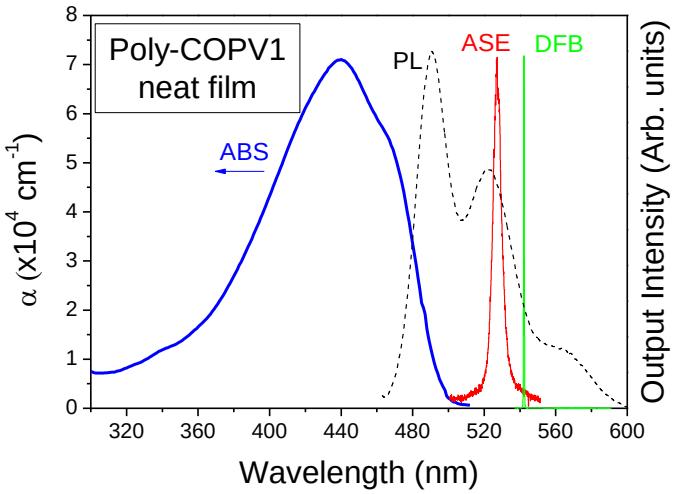

Figure 6.19.- ABS (thick solid line, left axis), PL, and ASE (dashed line and thin solid line, respectively; right axis) spectra for a neat film of poly-COPV1. The spectrum of a DFB laser based on this compound is also shown.

ASE appears at around 527 nm (threshold 4 kW/cm^2), considerably lower than COPV1 and only twice bigger that the best ASE result obtained with COPV compounds. The net gain coefficient has been determined at four different pump intensities: 3.9 kW/cm^2 (around threshold energy), 6.5 kW/cm^2, 18.2 kW/cm^2 and 34.8 kW/cm^2, obtaining g_{net} values of 21 cm^{-1}, 29 cm^{-1}, 33 cm^{-1}, 60 cm^{-1}, respectively (figure 6.20). These values are only slightly lower than those of state-of-the-art organic semiconductors.[12,123]

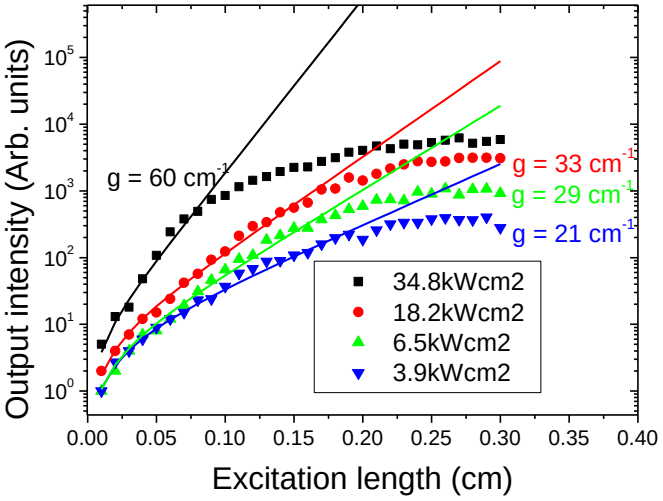

Figure 6.20.- Dependence of the emission intensity at the maximum of ASE on the excitation length at pump intensities of 3.9 kW/cm^2 (blue triangles), 6.5 kW/cm^2 (green stars), 18.2 kW/cm^2 (red circles), 34.8 kW/cm^2 (black squares). The solid lines are fits to the data using eq. (1.8).

Particularly remarkable is its ASE photostability halflife $\tau_{1/2}^{ASE}$ = 7.7 × 10^4 pp, (under soft pump conditions), which is two orders of magnitude larger than that of COPV1 dispersed in PS. Also remarkable is the high film PLQY: 67.7 studied in O_2, 70.5 studied in N_2. A DFB laser with a substructured DFB stamp, emitting at a wavelength of 542.2 nm, has shown a threshold as low as 1 kW/cm^2. ABS, PL, ASE and DFB spectra for the poly-COPV1 neat film are shown in figure 6.19. DFB threshold could be further improved by properly adjusting film thickness and period in order to obtain: high absorbance and DFB emission closer in wavelength to the ASE emission. Taking into account this low threshold, and the fact that the most powerful LEDs available in the market matches with its absorbance at 450 nm, this poly-COPV1 compound shows great prospect to be pumped with LEDs. Further work in this direction is currently under way.

6.5. Conclusions

- COPVs has demonstrated optimal properties as small-molecule aromatic dyes and conjugated polymer for laser action. These optimal properties are a consequence of the all-carbon, flat, large and rigid molecular COPV framework and also of the protection imparted by the bulky aryl substituents.

- The planar π-conjugated COPV core is ideal for maximal PL and consequently low ASE threshold.

- The *p*-octylphenyl substituents, provide solubility in common organic solvents, and hence processability as thin films by solution-based methods. They also impart protection of the π-system and further minimize chemical degradation and self-aggregation, in favor of very long laser operational lifetimes.

- The conjugation length of the investigated COPV oligomers investigated (COPV*n,* with *n* = 1-6 and the IPR-COPVs) shows the possibility of emission wavelength tuning by way of scalable chemical synthesis. Unlike aromatic dyes, they allow to systematically tune the emission laser wavelength over a wide range of the visible spectrum.

- Data for COPV*n*, with *n* = 1-6, compounds shows an inverse correlation between $\alpha[\lambda_{pump}]$ and $I_{th\text{-}ASE}$; all data except for COPV1-2 and highly doped COPV4 and COPV6 (larger $\alpha[\lambda_{pump}]$) are aligned on the same slope.

- The film PLQY for all COPV*n* compounds is extremely high (>90%) up to a dye doping rate in the film of 5 wt%. A PLQY decrease obtained in COPV4 and COPV6 at high dye concentration explains the saturation of $I_{th\text{-}ASE}$ observed at these concentrations.

- A g_{net} as high as 60 cm^{-1} has been obtained in a film containing 8 wt% of COPV6. This value is much superior to those obtained with other *p*-phenylenevinylene oligomers and PDIs dispersed in PS, while it is only about twice lower than state-of-the-art organic semiconductors.

- COPVs show an excellent photostability. In particular the ASE photostability of COPV6 in PS films (~10^5 pp) is several orders of magnitude better to those than other *p*-phenylenevinylene compounds, and even better than the best results reported for aromatic laser dyes doped in a polymer matrix.

- The inclusion of IPR substituents in COPV1 and COPV2 show a photostability improvement of around two times.

- COPV-based DFB lasers with resonators fabricated by different methods (T-NIL, HL or UV-NIL) have been demonstrated. It is remarkable the very low DFB threshold obtained with a 8 wt% COPV6 film, 0.7 ± 0.1 kW/cm^2, simultaneously with a very high operational device half-life under excitation two times above threshold of ~10^6 pump pulses. This threshold value is the lowest among the reported DFBs based on dye-doped polymer active materials, and very close to the requirements for LED pumping (around 0.3-0.5 kW/cm^2)

- The absorption spectrum of the polymer poly-COPV1 matches with the most powerful LEDs available in the market, which emit at 450 nm, and the low ASE threshold shown in this compound (3 kW/cm^2) make pumping with a LED feasible.

- We have demonstrated that DFB lasers with resonators engraved by HL over DCG layers deposited on top of the active films show an excellent performance, comparable to those of similar lasers based on gratings fabricated over inorganic substrates with the active film on top. This kind of DFB resonator offers the possibility to obtain large size devices (various centimeters) as well as to obtain wide wavelength tunability in a single device. Another advantage is that they are processed from water solutions, so they can be easily deposited and removed without damaging the active film placed underneath.

CHAPTER 5. DFB lasers for sensing applications

5.1. Introduction

5.2. DFB laser as bulk refractive index sensor

5.2.1. High sensitivity sensors based on very thin active films

5.2.2. DFB sensors with thick films and the use of TE_1 mode

5.2.3. Influence of film thickness on the ASE and DFB properties

5.2.4. Two-layer DFB laser (TiO_2/PDI-O doped PS over resonator)

5.3. DFB laser as biosensor

5.3.1 Biosensing capabilities

5.3.2 ErbB2 immunoassay

5.4. DFB laser to monitor solvent extraction upon thermal annealing

5.4.1. Solvent loss and wavelength shift as a function of annealing time

5.4.2. DFB sensor sensitivity

5.5. Conclusions

5.1. Introduction

This chapter describes the use of DFB sensors (based on PDI-O doped PS films) for different applications, as described in chapter 2. Firstly, we analyze the sensitivities and thresholds of some bulk refractive index DFB sensors (Λ = 376 nm), whose operation is based on detecting a shift in the laser wavelength upon the deposition of liquids of different refractive index, n_c. We have compared the properties of DFB sensors with different film thickness and have also analyzed the consequences of adding a top TiO_2 layer to the devices. Secondly, we demonstrate the applicability of one of the refractive index sensors mentioned before to detect a cancer biomarker, ErbB2. Finally, we have used a DFB laser (Λ = 368 nm) to monitor the extraction of the residual solvent content in the polymer film that constitutes itself the active film of the device. This sensor is used, particularly, to study the residual amount of toluene in PS films subjected to thermal treatments, by analyzing the wavelength shift produced in the device while the solvent is evaporated.

5.2. DFB laser as bulk refractive index sensor

5.2.1. High sensitivity sensors based on very thin active films

It is known that the sensitivity of this type of sensors increases when film thickness decreases, as illustrated in figure 5.1. This figure shows a calculation, through eq. (1.20), of λ_{Bragg} as a function of h_f (this parameter is included in n_{eff}) for a device exposed to air and water. As observed, the wavelength shift upon water deposition ($\Delta\lambda_{A\text{-}W}$) gets larger as h_f diminishes, due to the increase in the dispersion curve slope. The n_{eff} values used in this calculation were obtained by solving the propagation wave equation for the simplest possible model waveguide, consisting of a film of thickness h_f deposited over a planar fused silica substrate of infinite thickness (see section 1.3).[88,112] It is also assumed that the cover layer (air or water) has infinite thickness. The calculated cut-off thickness for the waveguide in air for the TE_0 and TE_1 modes (eq. 1.19) are respectively $h_{cut\text{-}off}$ (TE_0) = 149 nm and $h_{cut\text{-}off}$ (TE_1) = 600 nm. So, the election of h_f = 160 nm aimed to be just above $h_{cut\text{-}off}$ (TE_0).

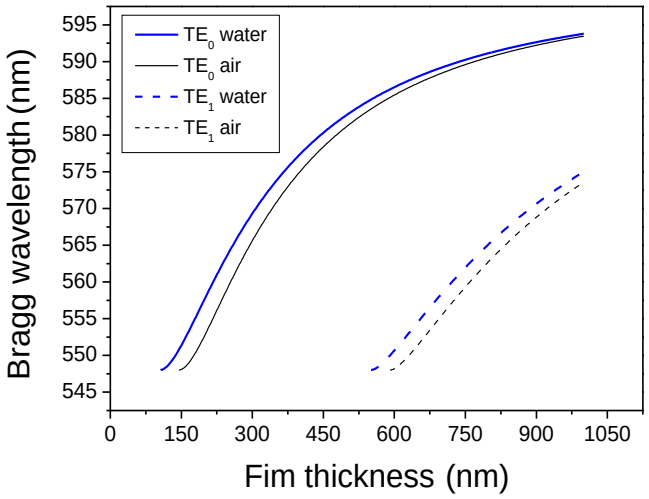

Figure 5.1.- Bragg wavelength versus active film thickness for single-layer DFB laser sensor. Calculation done through eq.(1.20) with n_{eff} values for TE_0 and TE_1 modes determined from the propagation wave equation considering the device exposed to air and water (full and dashed line, respectively).

As it has been explained above, the use of a very thin active film allows increasing the sensitivity. For this reason, we have first chosen h_f = 160 nm aimed to be just above $h_{cut\text{-}off}$ (TE_0). For this device, laser emission is associated to the TE_0 waveguide mode. The refractive index sensing capability of this sensor with h_f = 160 nm is illustrated in figure 5.2.a, which shows the experimental DFB spectra in air and after the deposition of liquids of different refractive index on top of the device. The wavelength shift upon water deposition ($\Delta\lambda_{A\text{-}W}$) is 4.2 nm. The sensor sensitivity near the refractive index value of 1.33 (the biological range) is *Sb* = 32 nm/RIU (see figure 5.2b). This *Sb* value is comparable to those reported for other single-layer waveguide DFB sensors (*Sb* = 20 nm/RIU at *n* = 1.33),[65,71] which have demonstrated their capability to detect biomolecules.[65,113] This indicates that the prepared PDI-O-based DFB sensors have sufficient sensitivity to be used for biomolecule detection, as we will show in section 5.3. It should be noted that these sensitivities can be further improved by including high refractive index layers on top of the laser device (see section 5.2.4) or by increasing the refractive index difference between active film and substrate, as recently demonstrated.[113] The sensor resolution, *r*, was calculated by analyzing, with the center mass model,[73] the peak corresponding to the case of water superstrate. Thus, from a set of 50 spectra, we determined a resolution of 0.8 pm and a LOD of 2.5×10^{-5} RIU. This LOD value is similar to that of photonic crystal sensors.[114,115]

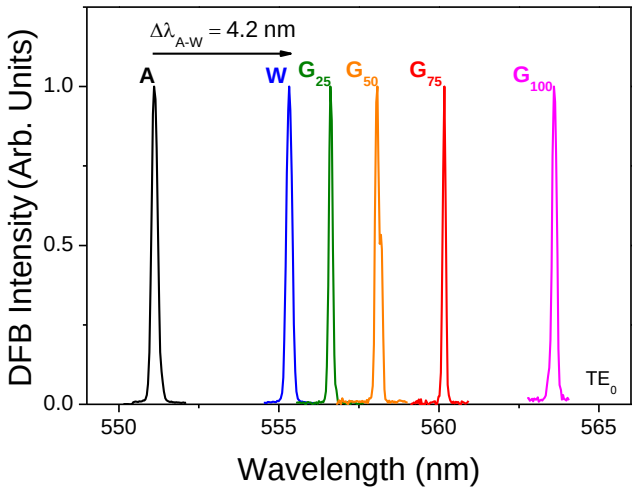

a)

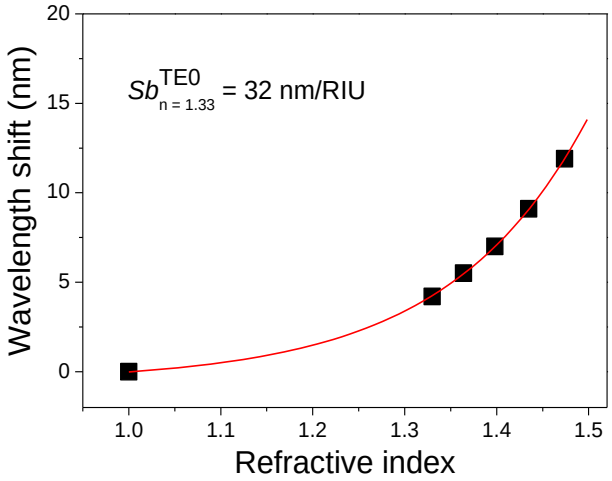

b)

Figure 5.2.- a) Laser spectra of a single-layer DFB sensor with h_f = 160 nm exposed to air and different liquids. Spectra (output DFB intensity, versus emission wavelength, from left to right correspond to air (A), water (W), and several aqueous solutions of glycerine –25 wt% (G_{25}), 50 wt% (G_{50}), 75 wt% (G_{75}) and pure glycerine (G_{100}) – on top of the device. b) Wavelength shift ($\Delta\lambda$) versus superstrate refractive index (n) and sensor sensitivity (Sb) determined in the biological range.

A drawback of using a very thin active film in the DFB laser is that the DFB threshold becomes larger and the operational lifetime becomes lower than those achievable with DFBs based on thicker films.[43,46] For this reason, in order to improve the DFB threshold and operational lifetime, devices with thicker active films were prepared. We first fabricated a laser with h_f = 180 nm, only slightly thicker than the one just discussed. The aim was to test how critical a change of thickness is in the sensor sensitivity and its threshold. Following the same procedure shown in figure 5.2.b, the sensor sensitivity in the biological range is *Sb* = 28 nm/RIU, only slightly inferior, while its threshold improves considerably, as discussed in detail in section 5.2.3.

5.2.2. DFB sensors with thick films and the use of TE_1 mode

The strategy followed here to obtain a device with low threshold and a long operational durability, while keeping a reasonable sensitivity, has been to prepare an even thicker film, particularly h_f = 850 nm, which supports two waveguide modes (TE_0 and TE_1). The idea is to make the DFB device operating at a wavelength associated to the TE_1 mode, whose dispersion curve for thick films has a larger slope than that of the TE_0 one (see figure 5.1), and therefore with better sensitivity.

The wavelength shift of the device with h_f = 850 nm upon water deposition, with respect to the one under air, was determined for both modes, TE_0 and TE_1 (see figure 5.3). Upon water deposition, the wavelength shift for the TE_1 mode is $\Delta\lambda_{A\text{-}W}$ = 1.3 nm, two times larger than that obtained with the TE_0 mode ($\Delta\lambda_{A\text{-}W}$ = 0.6 nm). The advantage of using the TE_1 mode is also reflected in its higher sensitivity value (figure 5.3, inset). Note that although this *Sb* value is smaller than that of devices based on thin films, its operational lifetime is significantly larger and its threshold is significantly lower, as we will show below. We remark this fact because for applications for which a very large sensitivity is not needed, but a low threshold and long device lifetime are required, the use of thick films would be a wise option.

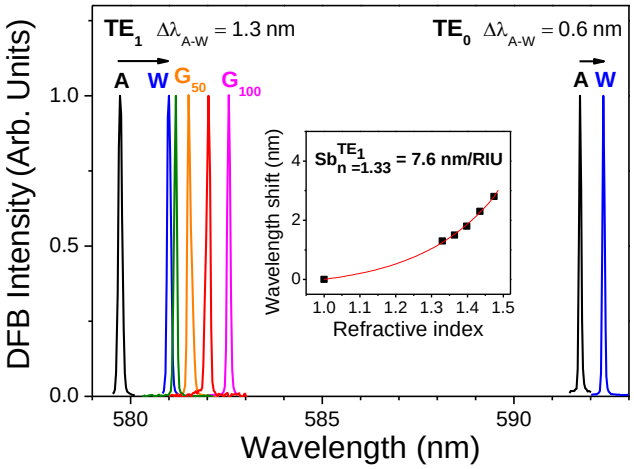

Figure 5.3.- Laser spectra of a single-layer DFB sensor with h_f = 850 nm exposed to air and different liquids. Spectra shown correspond to air (A), water (W), and several aqueous solutions of glycerine –25 wt% (G_{25}), 50 wt% (G_{50}), 75 wt% (G_{75}) and pure glycerine (G_{100}) – on top of the device. Each DFB spectrum consists of two peaks corresponding to the TE_1 and TE_0 waveguide modes. Inset: Wavelength shift of TE_1 mode versus superstrate refractive index and sensor sensitivity (*Sb*) determined in the biological range.

5.2.3. Influence of film thickness on the ASE and DFB properties

The effect on the DFB spectra and thresholds of changing h_f is analysed through figures 5.4 and 5.5, which show results for the three prepared devices (with h_f values of 160, 180 and 850 nm). ASE data correspond to films of the same characteristics of the DFB devices but deposited over substrates without gratings. The interest of studying also the ASE properties relies on the fact that the ASE wavelength practically does not change when h_f is varied, in contrast to the DFB wavelength, which is very sensitive to changes in h_f.[43] So, ASE analysis constitutes a useful tool to clarify the role of the waveguide mode confinement on the threshold.[88]

Let's first analyze the ASE results. The ASE spectrum (figure 5.4.a) red-shifts only slightly when film thickness increases, while the ASE threshold increases considerably ca. from 6 kW/cm^2 (for h_f = 850 nm) up to 120 kW/cm^2 when h_f is decreased down 160 nm (see figure 5.4.b). This is due to the lower absorption and therefore PL intensity of the latter, as well as to a poorer confinement of the waveguide mode.[88] As a consequence of having a higher threshold, the operational lifetime diminishes, given that the device needs to be pumped at a higher intensity and this parameter affects critically the photostability performance.[46,47] Indeed, the very large ASE photostability half-life value of 2×10^5 pp (under excitation two times above the ASE threshold) found for the 850 nm-thick film, decreases by around one

order of magnitude in the thinnest film. But this difference is not a material property dependent of film thickness, but a direct consequence of the higher threshold of the thin film, which requires a higher pumping intensity for operation and this parameter affects critically the photostability performance.[46,96]

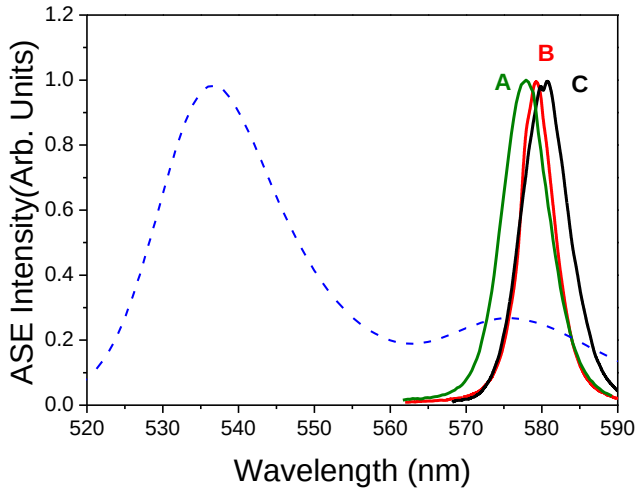

a)

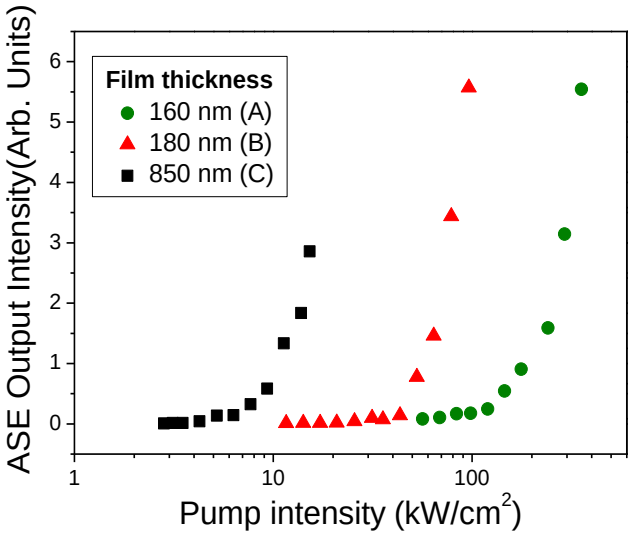

b)

Figure 5.4.- ASE properties for active films with different h_f values. Emission spectra and output intensity versus pump intensity curves for threshold determination are shown in (a) and (b) respectively. Shown data correspond to h_f = 160 nm (A: green line, circles), h_f = 180 nm (B: red line, triangles) and h_f = 850 nm (C: black line, squares), deposited over fused silica without gratings. The corresponding PL spectra are also shown (dashed blue line).

In the case of the DFB lasers, changes in h_f have an important effect on λ_{DFB} (figure 5.5a) due to the DFB grating. Thus, the analysis of the effect of changing h_f on the threshold, which is also quite drastic (figure 5.5.b) is more complex than in the ASE case. Devices with the thinnest films (h_f = 160 nm and h_f = 180 nm) show one single peak, associated with the TE_0 mode. Their thresholds are quite large (210 and 73 kW/cm^2, respectively) mainly because they emit far from the wavelength of maximum gain (given by the ASE wavelength), but it is also because waveguide mode confinement is poor, as previously shown by the ASE data. The important role of the waveguide mode confinement is confirmed by the fact that for the film with h_f = 850 nm, the threshold of the DFB peak associated to the TE_0 mode is only 20 kW/cm^2, although this one also emits at a wavelength far from the peak gain. Importantly, the lowest threshold was obtained for this thicker film, but for the DFB peak associated with TE_1 mode (3 kW/cm^2), due to its proximity to the peak gain.

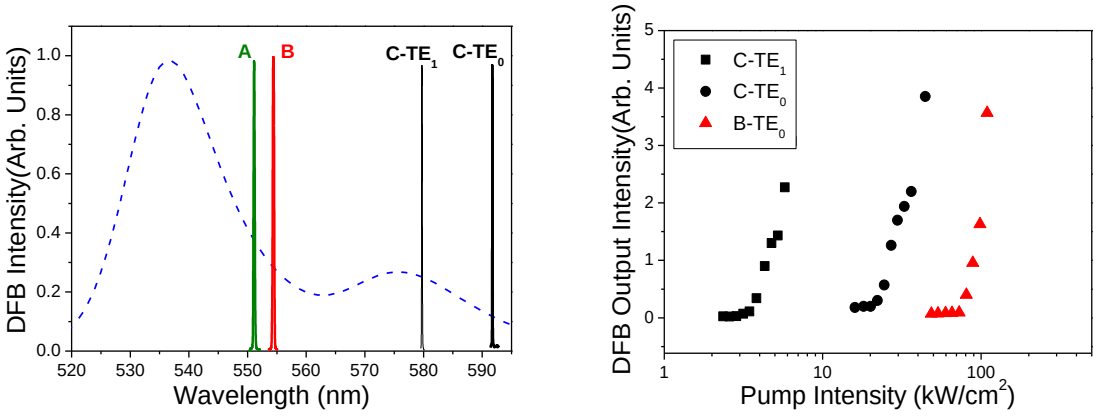

a) b)

Figure 5.5.- DFB properties for single-layer DFB sensors with different h_f values. Emission spectra and output intensity versus pump intensity curves for threshold determination are shown in (a) and (b) respectively. Shown data correspond to h_f = 160 nm (A: green line, circles), h_f = 180 nm (B: red line, triangles) and h_f = 850 nm (C: black line, squares), deposited over fused silica with gratings. The corresponding PL spectra are also shown (dashed blue line).

5.2.4. Two-layer DFB laser (TiO_2/PDI-O doped PS over resonator)

Here we discuss the effect on the sensor performance of depositing a high refractive index TiO_2 layer on top of the devices explained above. The strategy has demonstrated success for increasing the sensitivity of other DFB sensors.[23,24,72] In this sense, we have used a DFB laser device with h_f = 160 nm, such as the one whose data are shown in figure 5.2, but including a top 26 nm-thick TiO_2 layer (prepared in a MIDAS 450 semi-industrial vacuum chamber designed by IK4-TEKNIKER).

First of all, it should be noted that λ_{DFB} appears at a value of around 10 nm above the one obtained with the device without TiO_2 layer (see figure 5.6a). Upon water deposition, the shift in the emission wavelength is now $\Delta\lambda_{A\text{-}W}$ = 10.2 nm and the sensitivity *Sb* = 60 nm/RIU. These values are around two times larger than those obtained with devices without TiO_2. This *Sb* value is comparable to that reported by Vannahme et al.[72] (*Sb* = 70 nm/RIU, at *n* = 1.33) which performed a detailed investigation to optimize the thickness of the TiO_2 layer to obtain the maximum sensitivity.

The DFB spectra consist of a single peak associated with the TE_0 mode, except in the case of glycerine exposure which showed an additional peak corresponding to the TE_1 mode. The association of a given laser peak to a certain waveguide mode was done as in section 1.5 through eq. 1.20, although in this case the n_{eff} values could not be calculated in the frame of a waveguide film between two media of infinite thickness, because of the presence of the TiO_2 layer. Instead, a multilayer model was used.[93]

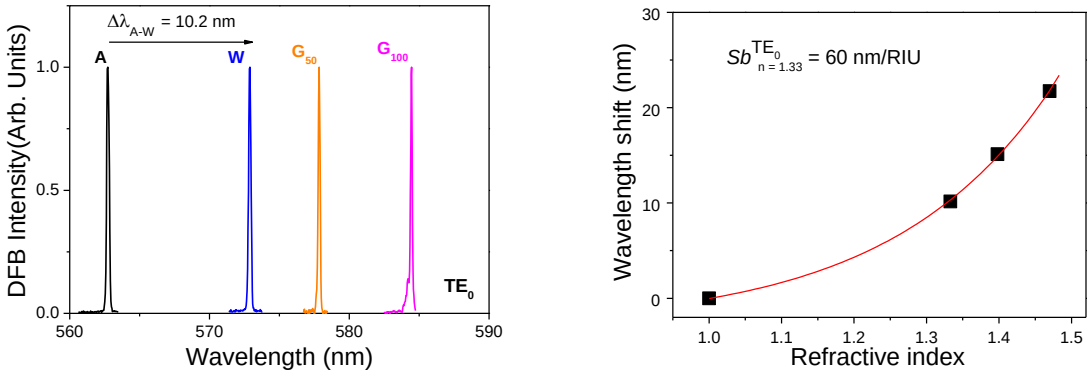

a) b)

Figure 5.6.- a) Laser spectra of two-layer DFB sensors (with top TiO_2 layer) exposed to air and different liquids. Spectra shown correspond to devices with h_f = 160 nm exposed to air (A), water (W), an aqueous solutions of glycerine at 50 wt% (G50) and pure glycerine (G100). Spectra shown in (a) correspond to TE_0 waveguide modes. The spectrum for G100 shows also a peak at 570 nm (not shown) associated to the TE_1 waveguide mode. b) Wavelength shift of TE_0 mode versus superstrate refractive index and sensor sensitivity (*Sb*) determined in the biological range.

The effect of including a top TiO_2 layer in the sensor structure has also been investigated for a DFB laser with h_f = 850 nm, which as discussed in previous section, are particularly interesting for their lower thresholds and higher operational lifetime. The DFB spectrum of such a device with h_f = 850 nm and the TiO_2 layer consists of several peaks associated with different waveguide modes (TE_1 and TE_2 in air; TE_1, TE_2 and TE_3 in water…; see figure 5.7, which makes the sensing capability analysis rather complicated.

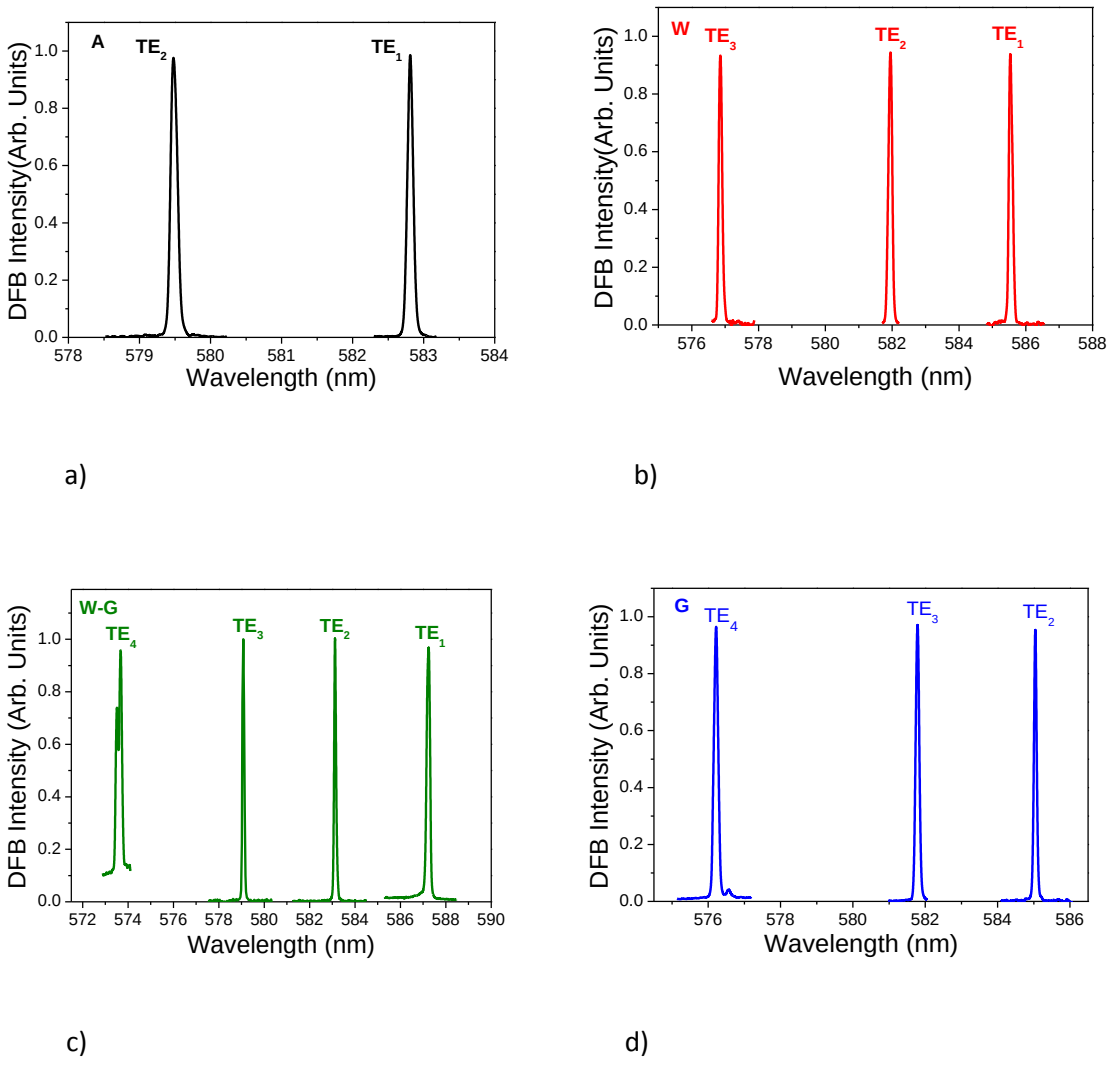

Figure 5.7.- Laser spectra of a two-layer TiO_2 (h = 26 nm)/PDI-O-doped PS (h_f = 850 nm) DFB sensor exposed to: (a) air, A; (b) water, W; (c) water-glycerine 50 wt%, W-G and (d) glycerine, G.

Only the TE_2 mode allows sensing ($\Delta\lambda_{A\text{-}W}$ = 2.5 nm and *Sb* = 16 nm/RIU) in the same range of refractive indexes used in previous devices studied in this work (figure 5.8), since it is the one appearing in all cases (in air, water, etc…). In accordance with the device based on a thin active film, the sensitivity also increases thanks to the inclusion of the TiO_2 layer. The existence of various DFB peaks due to the multimode character of these devices limits the interest of these devices in comparison to the ones showing only one DFB peak.

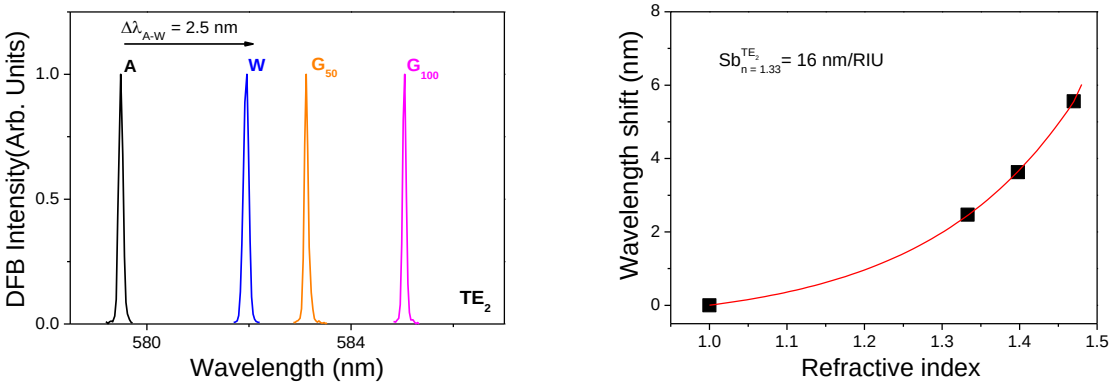

a) b)

Figure 5.8.- a) Spectra of TE_2 waveguide mode (peaks associated with other modes not shown) exposed to air (A), water (W), water-glycerine 50 wt% (W-G) and glycerine (G). b) The wavelength shift for the laser peak associated to TE_2 mode is plotted versus the superstrate refractive index for sensor sensitivity (*Sb*) determination in the biological range.

With regards to the effect on the laser threshold of the presence of the TiO_2 layer, it was observed that it becomes around two times larger than those of devices without TiO_2. This can be attributed to the presence of higher order modes, although a detailed interpretation of this issue is not an obvious task.

5.3. DFB laser as biosensor

A single-layer DFB with an active film with h_f = 160 nm such as the one explained in section 5.2.1, has been used to detect the ErbB2 protein biomarker. Specificity of the system to the ErbB2 protein biomarker, achieved by functionalizing the PS with anti-ErbB2 monoclonal antibodies, is demonstrated (see section 4.5.3). The used DFB sensor shows one single peak, that before functionalization appears at λ_{DFB} = 555.2 nm (see figure 5.2).

5.3.1 Biosensing capabilities

With the aim of proving the biosensing capabilities of the developed DFB lasers, an immunoassay for the detection of ErbB2 protein was developed (see section 4.5.3). This protein, as it has been commented in section 2.4.1, is an important oncogene relevant to certain aggressive types of breast cancer and its overexpression has been proved to serve as biomarker of the status and progression of the illness.[68] Given the label-free properties of the DFB sensing, a direct immunoassay was designed.

The emission wavelength of the laser was measured before and after the anti-ErbB2 functionalization (see figure 5.9). An average shift of 0.51 nm was obtained, similar to other protein immobilization methods employed for DFB biosensors.[24] When developing an immunoassay, it is always of the upmost importance to evaluate its specificity. For such purpose, incubation of the anti-ErbB2 DFB surface with BSA at a very high concentration (5 mg/mL) did not alter the emission wavelength of the DFB laser beyond the measurement uncertainty (see figure 5.9). This proved the correct formation of a specific anti-ErbB2 antibody monolayer on the surface. In figure 5.9 it is also shown, as an example, the spectrum after deposition of a solution with the ErbB2 protein at a concentration of 10 ng/ml.

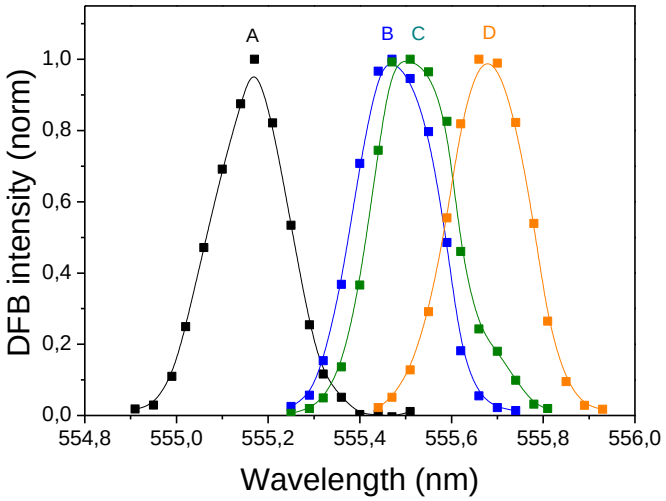

Figure 5.9.- DFB spectra of the sensor device in each step of the immunoassay. From left to right: (A) before functionalization, (B) after functionalization with antiErbB2, (C) after BSA blocking, (D) after analyte addition (ErbB2) at a concentration of 10 ng/ml. The symbols represent the collected experimental points.

The specificity and cross reactivity of the developed immunoassay was also tested using a solution of TNFα (incubated as BSA, see section 4.5.3), a related biomarker at a higher concentration (1 μg/mL) than those employed for the ErbB2 protein. As it can be seen in figure 5.10, where a positive sample of ErbB2 at 250 ng/mL is presented for comparison, the TNFα signal obtained was null, which proved the high specificity of the developed DFB biosensor. It can be seen that non-specific interactions due to large concentration of proteins are negligible, compared to the specific signal of low concentration ErbB2 positive samples.

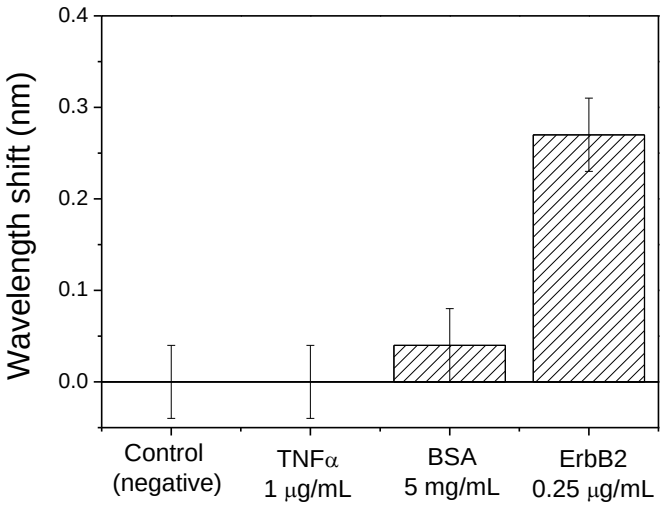

Figure 5.10.- Selectivity tests for the ErbB2 immunoassay.

5.3.2 ErbB2 immunoassay

Several DFB chips were prepared to run the direct binding ErbB2 immunoassay on their surface, as well as to obtain a calibration curve. Solutions of ErbB2 prepared on PBS buffer with 0, 2, 10, 250 and 10000 ng/mL concentrations were incubated during 2 hours in order to quantify their emission shift. The DFB spectrum for the case of 10 ng/ml has been included in figure 5.9 to illustrate the displacements with respect to spectra obtained in previous stages of the immunoassay. With the displacements obtained for the different concentrations, a calibration curve is obtained (figure 5.11). It is remarkable that even the lowest concentration of 2 ng/mL gave rise to a detectable wavelength shift. A LOD of 14 ng/mL was calculated as the concentration corresponding to a signal three times the standard deviation of the negative samples, that it is the samples with BSA. This was considered as the measurement error. To the best of our knowledge, this is the lowest concentration LOD value reported for a DFB-based protein biosensor. It is worth mentioning that the established clinical cut-off for the ErbB2 biomarker is 15 ng/mL.[116] Therefore, the result obtained with our biosensor probes its potential utility.

This LOD value is higher than that achievable with other types of sensors. For example, a LOD as low as 26 pg/mL has been obtained for the ErbB2 biomarker in diluted samples using a highly sensitive amperometric magnetoimmunosensor.[117] However, DFB laser biosensing represents a cost-effective way to detect biomolecules and the DFB laser can be made entirely in polymer[20] or even be completely biocompatible.[95]

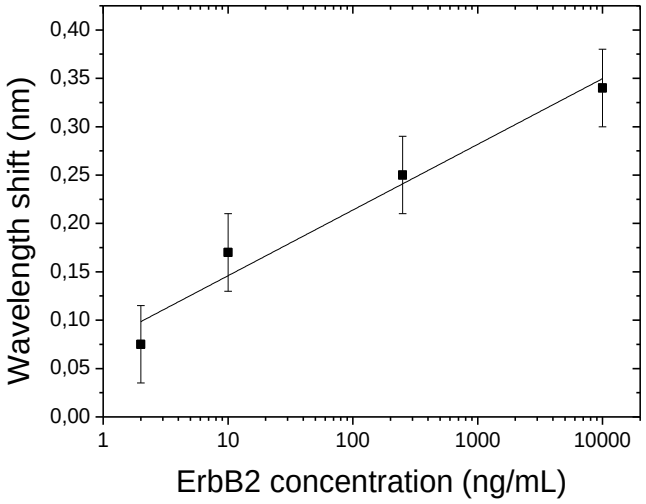

Figure 5.11.- Calibration curve constructed for the detection of ErbB2 with an organic DFB laser. The concentrations used are 2, 10, 250 and 10,000 ng/mL. The concentration LOD was estimated in 14 ng/mL.

5.4. DFB laser to monitor solvent extraction upon thermal annealing

5.4.1. Solvent loss and wavelength shift as a function of annealing time

The toluene mass content in fresh (right after deposition) PS films with h_f ~ 1000 nm is ~ 60 μg (6.5 vol %). This was measured as described in section 4.1.2. Half of this content is evaporated in the first 30 min and the rest is evaporated during around 6 h, until the remaining solvent is very small, 0.3 μg. A small amount of toluene, 0.1 μg (measured by TD method), remains in the samples after 24 h treatments. The evolution of the residual mass of solvent in the film for different annealing times is shown in figure 5.12.

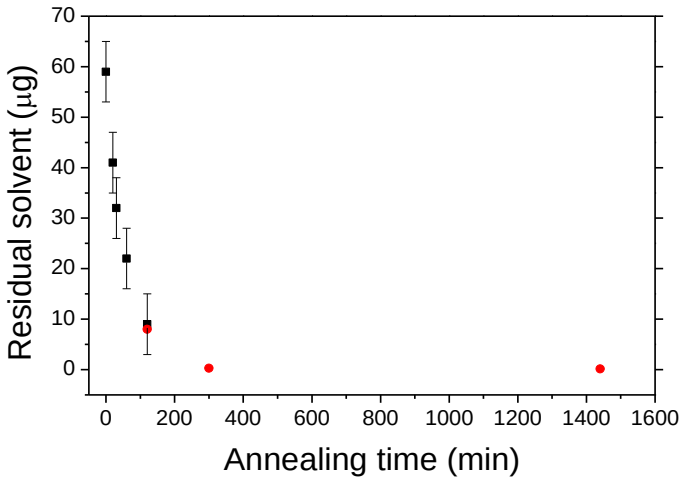

Figure 5.12.-Residual solvent in the sample as a function of the annealing time, measured with a microbalance and a thermobalance (squares) or by thermal desorption (TD), with a gas chromatography (GC) coupled a mass spectrometer (circles).

Laser emission spectra of a DFB laser after different thermal treatment times, *t*, is shown in figure 5.13.a (DFB with type I geometry according to figure 1.7). The laser emission wavelength (λ_{DFB}), which is around 581.5 nm for the fresh sample, blue shifts as *t* increases. Figure 5.13.b displays λ_{DFB} as a function of *t* for one sample. Uncertainty is included in the figure as error bars. A fast decay in λ_{DFB} is observed in the first 30 minutes and then, a slow decrease during several hours.

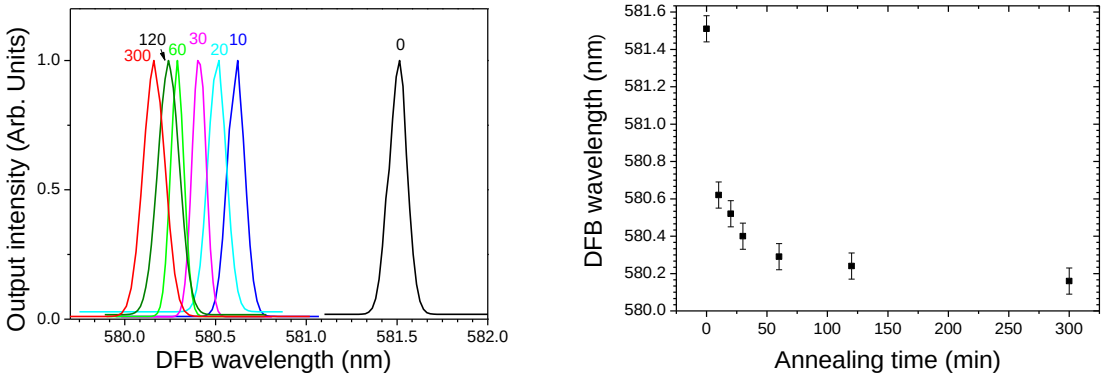

a) b)

Figure 5.13.- (a) Laser spectra of one organic DFB laser subjected to thermal treatments in an oven at 90 ºC at different thermal treatments times, *t* , (0, 10, 20, 30, 60, 120 and 300 min); (b) Emission DFB wavelength, λ_{DFB}, versus *t* for the same sample.

5.4.2. DFB sensor sensitivity

By combining data from figures 5.12 and 5.13.b, the DFB wavelength shifts, $\lambda_{s\text{-DFB}}$ at different treatment times (with respect to the λ_{DFB} value of the fresh sample) have been represented in figure 5.14 as a function of the solvent loss (Δm_L). Solvent loss is calculated as toluene mass in the fresh sample (60 μg) minus the residual solvent. This representation is useful to assess the sensitivity of the laser device used here as a sensor of the amount of solvent eliminated. Two regimes can be distinguished: regime I, with a high sensitivity of $\Delta\lambda_{s\text{-DFB}}$ /Δm_L ~0.050 nm/μg, during which approximately the first half of the solvent is extracted; and regime II, with a lower sensitivity ($\Delta\lambda_{s\text{-DFB}}$ /Δm_L ~ 0.0075 nm/μg), which corresponds to the slow extraction of the second half of solvent. Note that measurements in the first part of regime I (approximately the first 5 min), are difficult to perform mainly because of the temperature variations during the time needed to reach the steady-state inside and outside the oven.

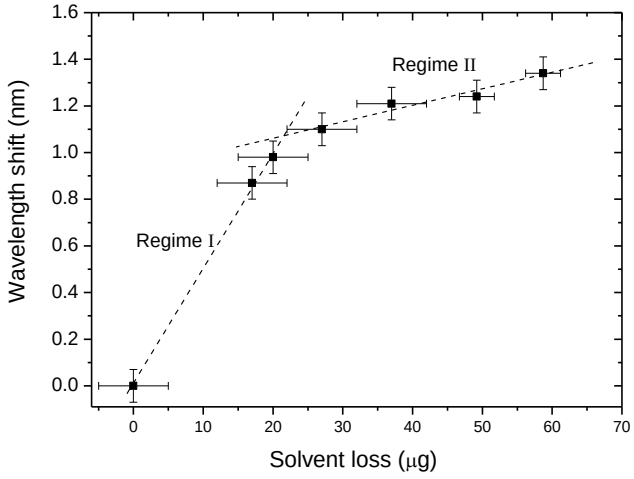

Figure 5.14.- DFB wavelength shift as a function of solvent loss with respect to the values of the fresh sample. Dashed lines are guides to the eye.

The observation of shifts in λ_{DFB} upon solvent elimination is because of changes in the active film thickness (h_f) and refractive index (n_f), as indicated by measurements of these two parameters (see Table 5.1). The average h_f value of the fresh samples is ~ 1000 nm. After 30 min in the oven it quickly decreases down to ~ 990 nm, a value approximately equal to that obtained with an annealing time longer than two hours. On the other hand, n_f decreases gradually in the range where h_f is constant. Besides, the n_f value after an annealing time of 30 min is approximately equidistant between the average value obtained for the fresh sample, and that corresponding to a sample annealed during 6 h. From these measurements, it can be concluded that the shift $\lambda_{s\text{-DFB}}$ in the regime I is due to variations in both h_f and n_f, although with a stronger contribution of the former. On the other hand, in

regime II, h_f is practically invariant with t, while n_f keeps decreasing as in regime I. This explains the higher sensitivity of the sensors observed in the regime I respect to that of regime II.

Table 5.1 includes also theoretical values of the effective index and the laser emission wavelength. The calculated n_{eff} values (n_{eff}^{calc}) were obtained by solving the propagation wave equation for the TE_0 mode (see section 1.3). Once n_{eff}^{calc} is known, the corresponding λ_{Bragg} value (λ_{Bragg}^{calc}) can be calculated directly from eq. 1.20. It can be seen that the experimental and theoretical laser wavelength shift values are in very good agreement (error in λ_{Bragg}^{calc} is ± 0.10 nm).

t (min)	**n_f**	**h_f (nm)**	**λ_{DFB} (nm)**	**$\Delta\lambda_{s\text{-}DFB}$ (nm)**	**n_{eff}^{calc}**	**λ_{Bragg}^{calc} (nm)**	**$\Delta\lambda_{s\text{-}Bragg}^{calc}$ (nm)**
0 (Fresh sample)	1.5961	1063	581.50	0	1.58007	581.46	0
30	1.5953	992	580.40	1.10	1.57734	580.46	1.00
120	1.5949	991	580.26	1.24	1.57691	580.30	1.16
360	1.5946	991	580.16	1.34	1.57662	580.19	1.27

Table 5.1-. Experimental parameters: annealing time (t), active film refractive index (n_f), active film thickness (h_f), DFB wavelength (λ_{DFB}) and DFB wavelength shift ($\Delta\lambda_{s\text{-}DFB}$). Theoretical parameters: calculated effective index (n_{eff}^{calc}), theoretical laser wavelength (λ_{Bragg}^{calc}) and theoretical laser wavelength shift ($\Delta\lambda_{s\text{-}Bragg}^{calc}$).

5.5. Conclusions

5.5.1. DFB lasers as bulk refractive index sensors

- We have demonstrated that organic DFB laser sensors consisting of active films of PS doped with the PDI-O laser dye have an excellent photostability under operation in ambient conditions and a relatively low threshold.

- Their feasibility as bulk refractive index sensors as well as their sensitivity has been investigated through the changes observed in their laser emission wavelength upon exposure to different liquid superstrates: distilled water, aqueous solutions of glycerine and pure glycerine.

- A very thin film (h_f = 160 nm) device has shown a sensitivity value (Sb = 32 nm/RIU) comparable to other single-layer DFB sensors reported in the literature, while its threshold is relatively high (I_{th}^{DFB} = 210 kW/cm^2) and its operational durability moderate ($\tau_{1/2} \sim 10^4$ pp). A slight increase of thickness (h_f = 180 nm) has allowed decreasing the threshold by three times, while its sensitivity diminishes only slightly (Sb = 28 nm/RIU). The increase of h_f up to around 850 nm allows improving considerably the laser threshold (I_{th}^{DFB} = 20 kW/cm^2) and the operational durability ($\tau_{1/2} \sim 10^5$ pp), although the sensitivity decreases (Sb = 7.6 nm/RIU). In this case the overall performance is several times better when the sensor operates at the wavelength corresponding to TE_1 mode.

- The inclusion of a high refractive index TiO_2 layer on top of the sensor structure improves the sensitivity by around two times, although in the case of devices based on thick films, the sensor operation is complicated by the appearance of many peaks associated with high order waveguide modes.

5.5.2. DFB lasers as biosensors

- The feasibility of a thin film DFB sensor based on PDI-O-doped PS active film, such as the one explained in previous section, as a label-free sensor capable of detecting a cancer biomarker (ErbB2) has been demonstrated.

- Anti-ErbB2 monoclonal antibodies have been used to functionalize the PS active film. Incubation of the anti-ErbB2 surface with BSA protein ensures the specific anti-ErbB2 antibody monolayer on the surface.

- The specificity and cross-reactivity of the developed immunoassay has been demonstrated by using TNFα biomarker.

- The sensor specificity and the LOD (14 ng/ml) obtained for ErbB2 detection opens the possibility to use organic DFB lasers for clinical applications.

5.5.3. DFB lasers to monitor solvent extraction upon thermal annealing

- We have demonstrated the use of a PDI-doped PS DFB laser to monitor, with high precision (±2.5 μg), the amount of solvent extracted from a polymer film, as a function of the time of the thermal treatment at which the film is subject after its deposition by the spin coating technique. The polymer film under consideration is the active film of the DFB device.

- Half of the initial solvent content in the film, that of the fresh sample (not thermally annealed), is evaporated during the first 30 min of thermal treatment. Solvent elimination produced a blue shift of the DFB laser wavelength. The other half of solvent is evaporated slowly, along 6h, until the remaining solvent amount is very small.

- By representing the DFB wavelength shift as a function of the solvent loss, as a consequence of the thermal treatment two regimes can be distinguished: in regime I, λ_{DFB} changes rapidly (high sensitivity, $\Delta\lambda_{s\text{-}DFB}/\Delta m_L$ ~0.050 nm/μg) mainly because of a decrease of $h_{f,}$ and to a minor extent also because of a decrease of n_f; in regime II, in which λ_{DFB} varies slightly (low sensitivity, ($\Delta\lambda_{s\text{-}DFB}/\Delta m_L$ ~ 0.0075 nm/μg), h_f remains constant and n_f still decreases.

- A very good agreement between experimental λ_{DFB} and calculated λ_{Bragg}^{calc}, as a function of the thermal treatment time, has been found.

III. RESULTS

CHAPTER 5. DFB laser for sensing applications

CHAPTER 6. Carbon-bridged oligo(*p*-phenylenevinylene)s (COPVs) as novel laser materials

CHAPTER 7. General conclusions and future research